Optimising shape analysis to quantify volcanic ash morphology

E.J. Liu*, K.V. Cashman, A.C. Rust

Department of Earth Sciences, University of Bristol, Wills Memorial Building, Bristol BS8 1RJ, UK

ARTICLE INFO

ABSTRACT

Accurate measurements of volcanic ash morphology are critical to improving both our understanding of fragmentation processes and our ability to predict particle behaviour. In this study, we present new ways to choose and apply shape parameters relevant to volcanic ash characterisation. First, we compare shape measurements from different imaging techniques, including cross-sectional (2-D) and projected area images, and discuss their respective applications. We then focus on specific information that can be obtained from shape analysis of 2-D images. Using cluster analysis as an unbiased method to identify key controls on particle morphology, we find that four shape parameters – solidity, convexity, axial ratio, and form factor – can effectively account for the morphological variance within most ash samples. Importantly, these parameters are scaled to values between 0 and 1, and therefore contribute evenly to discrimination diagrams. In particular, co-variation in convexity and solidity can be used to distinguish different juvenile ash components based on characteristic bubble properties. By reducing observations of natural samples to simplified ash geometries, we quantify morphological changes associated with variations in the relative size and shape of bubbles and particles. Using this relationship, we assess the potential application of size-dependent shape analysis for inferring the underlying bubble size distribution, and thus the pre-fragmentation conditions. Finally, we show that particle shape analysis that includes the full range of available grain sizes can contribute not only measurements of particle size and shape, but also information on size-dependent densities.

1. Introduction

Particle morphology is analysed in many fields of the physical sciences. Regardless of the material, the shapes of particles record the processes responsible for their generation in unrivalled detail, and control particle behaviour and interaction. These two applications are far from mutually exclusive, as accurate predictions of particle behaviour require a fundamental understanding of mechanisms by which they form. Shape measurements are therefore key to improving our understanding of the origin and evolution of fragmental particles [10,22,50,67,80,81], to defining the material properties of the fragmented material [25], and to predicting particle behaviour, such as settling or radiative/scattering properties [1,4,45,53,69].

Volcanic ash, in particular, encompasses a diverse spectrum of (often extreme) shapes, each with different physical properties and behaviours. Understanding the link between morphological heterogeneity and aerodynamic behaviour is a key challenge for our ability to forecast ash dispersal [21,24]. The shapes of juvenile ash particles also reflect the fragmentation mechanisms operating during an eruption, which are in turn controlled by the magma properties (such as viscosity, temperature, and composition) and the conditions under which the magma ascends and erupts (e.g. [17,22,33,34,49,70,79]). Many questions remain, however, regarding how magma fragments, and particularly the roles of bubbles and crystals in controlling the fragmentation process [15,30,70]. Shape analysis provides a valuable, yet under-utilised, tool to decipher the generative mechanisms responsible for ash production. Although shape parameters are now commonly used to distinguish ash from different eruption styles (e.g., magmatic vs. hydromagmatic fragmentation; [10]), rigorous assessment of the generality of these relationships is lacking. Furthermore, differences in how shape parameters are defined and measured, and in the criteria by which parameters are chosen to address specific questions, often preclude direct comparison of existing shape data within the literature [47].

This study provides a quantitative assessment of shape analysis for the purpose of understanding the origin and characteristics of volcanic ash. To place our results in context, we first review previous applications of shape analysis in ash studies, and the evolution of shape measurements in response to technological advances. We then
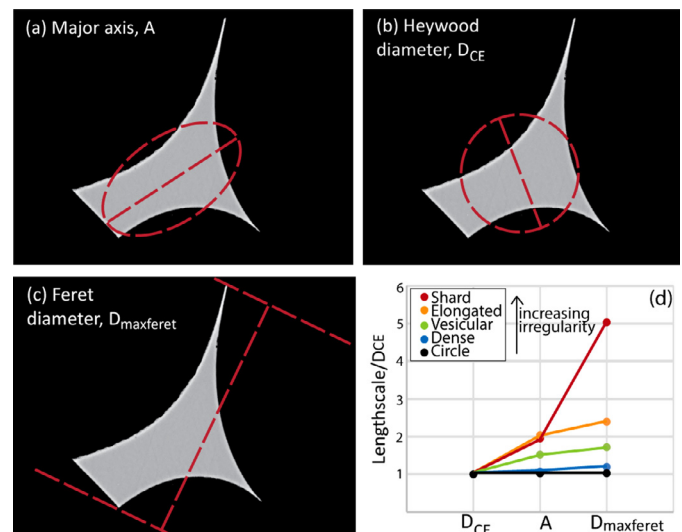
* Corresponding author. Tel.: +44 (0) 117 954 5400.
  E-mail address: emma.liu@bristol.ac.uk (E.J. Liu).

introduce our reference datasets, which include ash samples from a range of eruptive styles, including the recent Icelandic eruptions of Eyjafjallajökull (2010) and Grímsvötn (2011). The spectrum of ash morphologies enables us to evaluate the sensitivity of different shape parameters to methods of image acquisition and to assess the conditions required to accurately measure particle shapes from 2-D images. Using our optimised methodology, we then illustrate how shape analysis can be applied to specific volcanological questions related to ash formation. In particular, we relate shape parameter measurements to specific bubble textures, and show how shape changes between different particle size fractions can be linked to the size distribution of bubbles. Although based on the analysis of volcanic ash, the insights presented in this study have broader applicability to studies of fragmentation and particle behaviour, both within and beyond the field of volcanology.

2. Background

2.1. Shape parameterisation

Particle shape parameters provide quantitative and reproducible measures of shape that minimise the subjectivity associated with descriptive terminology and enable direct comparison amongst particles (or particle populations). Although the terms 'shape parameter' and 'shape factor' are often used synonymously, to avoid confusion with specific parameters of the same name (e.g., the Shape Factor of Wilson and Huang [92] or Dellino et al. [21,23]) we use the term 'shape parameter (SP)' when discussing quantitative shape descriptors more generally. Whilst a perfect sphere can be uniquely described by a single property – its diameter – irregularly-shaped particles require measurements of multiple dimensions [8]. Simple SPs are non-dimensional ratios of various measures of particle size – such as diameter, area and perimeter – and often quantify irregularity by comparing the shape of a particle to that of a standard reference shape (Tables 1 and 2; Fig. 1). Individual simple SPs are sensitive to specific aspects of particle morphology (such as elongation or surface

Fig. 1. Particle size measurements. The influence of different size measures on the apparent particle diameter. (a–c) Various size measures used to quantify particle diameter. (d) Variation in diameter measurements (normalised to the Heywood diameter, D_{CE}) for ash particles with a range of morphologies.

roughness), but can be combined to form compound SPs that provide more general measures of overall 'irregularity'.

The earliest simple SPs have their origins in sedimentology, and were developed to predict the hydraulic behaviour of non-spherical grains [3,11,42,78,87,90,91,94]; reviewed in Barrett [5]. Caliper measurements of three orthogonal particle axes – a, b, and c (*sensu* [90] and others) or S, I, and L (*sensu* [78]) – were used to calculate, for example, the Corey Shape Factor (CSF = $\frac{c}{\sqrt{ab}}$), a correction used to determine particle terminal velocity (V_T; [14,41]). By measuring V_T for volcanic ash grains of varying shape and texture, Wilson and Huang [92] demonstrated a similar shape-dependency for ash particle settling, but suggested that the Shape Factor, F ($F = b + c/2a$), provided a more effective shape correction for irregular ash particles. These early shape parameters effectively quantify variation in particle form/elongation, but neglect the contribution of other morphological properties, such as surface roughness, to overall particle irregularity and the influence of this on particle aerodynamics [8,14,19].

Advances in particle imaging capabilities and computer processing during the 1990s revolutionised shape analysis. The ability to compute particle dimensions directly from 2-D images enabled rapid analysis of much larger sample sizes than had been previously possible by manual measurements [72]. Furthermore, with the transition to shape analysis based on image processing came the definition of increasingly complex shape parameters; measurements were no longer restricted to those of the main particle axes and properties such as particle area, perimeter, bounding rectangle, and convex hull could be determined with accuracy. Automated methods also reduced operator bias and uncertainty in defining orthogonal axes. Shape analysis by image processing has also introduced a new consideration: how to best acquire images for maximum accuracy (Section 4.3) and, more fundamentally, how to choose the most appropriate perspective from which to view the particles (e.g., the projected area 'silhouette', or a cross-sectional slice). As discussed in Section 4.2, the choice of imaging perspective pre-determines the final shape parameter values, which cannot be directly compared between different imaging methods.

Ambiguities in measuring size is a significant source of uncertainty in the calculation of SPs. Particle diameter, for example, has been variably defined as the Feret diameter ($D_{MaxFeret}$; maximum distance between two parallel lines tangential to the particle outline),

Table 1
Summary of abbreviations.

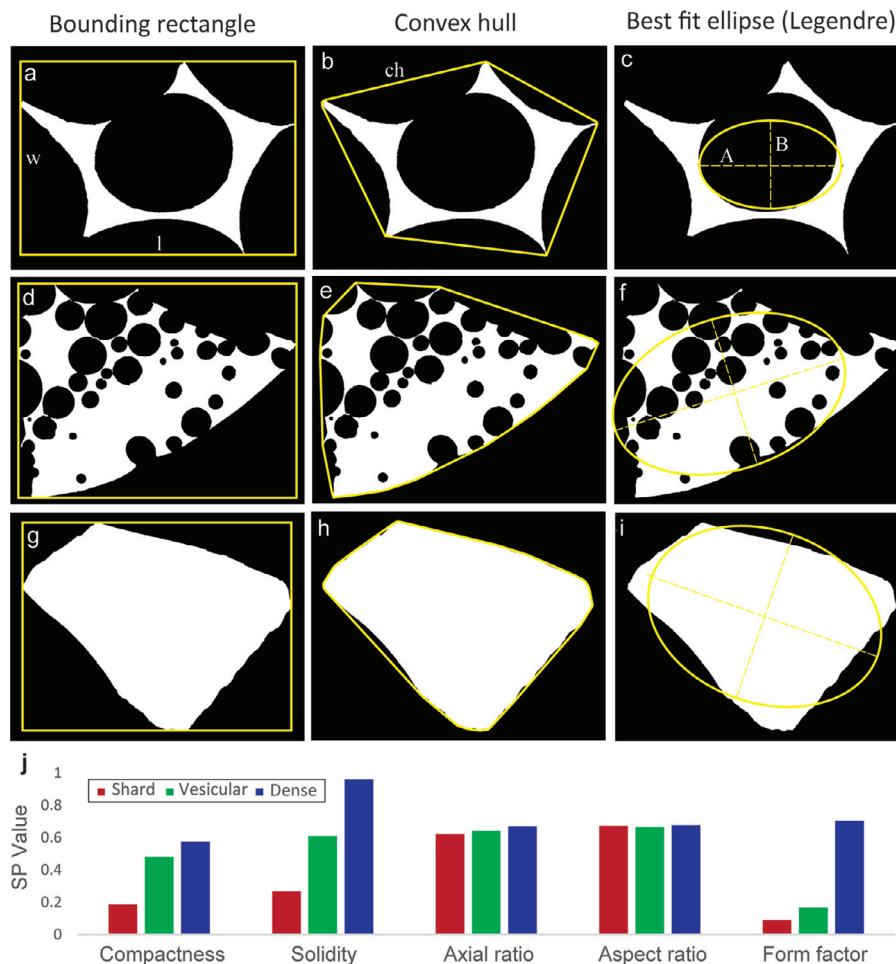| Symbol	Definition
A_p	Area of the particle
A_{ch}	Area of the convex hull
P_p	Perimeter of the particle
P_{ch}	Perimeter of the convex hull
l	Length of bounding rectangle
w	Width of bounding rectangle
A	Major axis of best-fit ellipse
B	Minor axis of best-fit ellipse
L_b	Maximum dimension parallel to major axis of the best-fit ellipse
W_b	Maximum dimension parallel to minor axis of the best-fit ellipse
L, I, S	Long, intermediate, and short caliper axes
SA	Surface area of the particle
SA_{sph}	Surface area of equivalent volume sphere
D_{sph}	Diameter of volume equivalent sphere
$D_{MaxFeret}$	Maximum Feret diameter
$D_{MinFeret}$	Minimum Feret diameter
MIP	Mean intercept perpendicular
D_{CE}	Diameter of equivalent area circle (Heywood diameter)
L_G	Geodesic length
E	Geodesic thickness
D_i	Diameter of maximum inscribing circle
D_c	Diameter of minimum circumscribing circle
n	Number of particles
K	Number of perimeter-intersecting concavities
r	Radius of intersecting concavities
A_c	Area of intersecting concavities within the convex hull
D_b/D_p	Ratio of bubble to particle diameters
B_n	Number of intersecting bubbles

Table 2
Summary of shape parameter definitions and nomenclature. All abbreviations are detailed in Table 1.

Shape parameter (SP)	Abbreviation	Formula	Sensitivity	References	Alternative nomenclature
Form factor	FF	$\frac{4\pi A_p}{P_p^2}$	Form and roughness	[2,19,20,28,32,44,48,49,65,73]	Sphericity [1,7,56,69] Roundness [27,50,54] Circularity [9,18,35]; HS circularity ([47]; Malvern application note) Shape factor [6,76] Cox circularity [4]
Circularity	Circ	$\frac{P_p}{2\sqrt{\pi A_p}}$	Form and roughness	[10,21–23,25,39,47,58–60]	Shape factor [36]; Particle irregularity [57]
Solidity	SLD	$\frac{A_p}{A_{ch}}$	Roughness (morphological)	[18,49]	
Convexity	CVX	$\frac{P_{ch}}{P_p}$	Roughness (textural)	[65]; Malvern application note; [9,35,49]	Roughness [69] $\frac{A_p}{A_p+A_{ch}}$ [27]
Convexity_feret	CVX_f	$\frac{\pi D_{maxferet}}{P}$	Roughness (textural)	[32]	
Rectangularity	RT	$\frac{P_p}{2l+2w}$	Roughness (textural)	[2,10,17,22,25,39,47,58,60]	$\frac{P_p}{2A+2B}$ [19]
Compactness	CP	$\frac{A_p}{(lw)}$	Roughness (morphological)	[2,10,17,22,39,46,47,58,59,60]	$\frac{A_p}{(AB)}$ [19] $\frac{4\pi A_p}{P_{ch}^2}$ [69] $\frac{((\frac{4}{\pi})A_p)^2}{A}$ [28]
Aspect ratio	AR	$\frac{D_{minferet}}{D_{maxferet}}$	Form	[2,32,36,60,65,69]	$\frac{B}{A}$ [18,19,28,54,56,66,71,76] $\frac{L_b}{W_b}$ [47]
Axial ratio	AxlR	$\frac{B}{A}$	Form	[35,49]	Aspect ratio [19,28,54,56,66,71,76] Ellipse aspect ratio [18] Ellipticity [54]
Elongation	El	$\frac{D_{maxferet}^2}{A}$	Form	[46]	$1-\frac{L_b}{W_b}$ [47] $\frac{D_{maxferet}}{MIP}$ [10,22,25,39,58,60] $\frac{L_c}{E}$ [65] $\log_2(\frac{A}{B})$ [44,54] $\frac{A_p}{D_{maxferet}}$ [17] $\frac{4A_p}{\pi A^2}$ [28]
Roundness	RD	$\frac{4A_p}{\pi D_{maxferet}^2}$	Form	[32,65]	
Defect area	DeltA	$(\frac{A_{ch}-A_p}{A_p})$	Roughness (morphological)	[35,36]	
Paris factor	PF	$2(\frac{P_p-P_{ch}}{P_{ch}})$	Roughness (textural)	[35–37]	
Extent	Ext	$\frac{A_p}{D_{maxferet}D_{minferet}}$	Roughness (morphological)	[65]	
Concavity index	CI	$\sqrt{(1-\mathrm{SLD})^2+(1-\mathrm{CVX})^2}$	Roughness (combined)	[49]	

major axis (long axis of the best fit ellipse), or Heywood diameter (D_H; the diameter of a circle of equivalent area to that of the particle; Table 1; Fig. 1). Note that although D_H removes the need to define a long axis, it is not a physically measurable particle dimension. For a sphere (or circle in 2-D), the diameter is identical regardless of the measurement method. However, as particle morphology becomes increasingly irregular, the diameter measurements obtained using the different definitions become increasingly divergent (Fig. 1d). Importantly, the most practical definition of the long axis for manual measurements – $D_{MaxFeret}$ – is inherently flawed for rectangular particle geometries, where the longest dimension passes diagonally through opposite corners. The major and minor axes of the best-fit Legendre ellipse, in contrast, provide a measure of diameter valid for all particle geometries because the axes are oriented to intersect through the centroid and are aligned along the particle's moments of inertia.

Within the volcanological literature there are a number of further SP considerations. Many SPs share the same definition but are assigned different names *or* SPs with different definitions are referred to by the same name (Table 2; [47]). Critically, the definitions of SPs determined using manufacturer-provided software may be buried in the documentation. Also, shape irregularity is commonly measured with reference to a fully compact form. The most common reference shapes are a circle/ellipse of equivalent area, a bounding rectangle or a bounding convex hull (Fig. 2). When using a standard geometric shape as a reference, the difference between the particle outline and the reference shape depends on both *form* and *roughness*. Compact particles (with low roughness) can be well described with reference to simple geometric shapes, and thus rectangularity and compactness are commonly used to measure deviation from the bounding rectangle (Table 2; e.g. [10,22]). A caveat for this approach is that in most image analysis software, the bounding rectangle is defined by the leftmost/rightmost and uppermost/lowermost pixels of a particle in an *X–Y* Cartesian reference frame (Fig. 2), making the resulting shape values dependent on orientation, and rotating the bounding box to align with the particle major axis may be non-trivial. For highly irregular particles, the convex hull is the closest approximation to a compact form and has the advantage of being orientation-independent. Finally, simple shape parameters are often scaled to values between 0 and 1, where values of 1 represent the fully compact shapes (i.e. the reference shapes). Some parameter definitions, however, are unbounded and extend from 1 to ∞ (again 1 represents fully the compact shape). Bounded shape parameters allow the total variance (and thus the contribution of any particular parameter to the overall measure of irregularity) to be held constant for all parameters, and are therefore encouraged [47]. This is particularly important when shape data are used either in compound shape parameters or for statistical tests such as cluster and/or cladistics analysis, where

Fig. 2. Selecting an appropriate reference shape. The influence of reference shape on shape parameter measurements, for (a–c) a bubble shard, (d–f) a vesicular particle, and (g–i) a dense fragment; (j) histograms showing shape measurements of the three ash particle images (of varying vesicularity). When bubbles are controlling ash morphology, solidity (referenced to the convex hull) distinguishes most effectively between the three particles, whilst axial/aspect ratio is least effective.

calculated Euclidean distances are sensitive to differences in scale and directionality.

2.2. Volcanological applications of computed shape analysis

The link between volcanic ash morphology and eruption style has long been recognised in volcanology. Whilst early descriptions of volcanic ash particles were largely qualitative, and used terms such as blocky, fusiform, cuspate, and moss-like to characterise distinctive external features [33,34,88,93], computed shape analysis is now used in volcanology to discriminate amongst ash particles of distinct morphologies (e.g. [17]), different origins (e.g. [22,23,39,47,49,51,58–60]) and different aerodynamic properties (e.g. [4,19,21,52,68,69]). An important step forward in the use of shape analysis to address questions of volcanic ash fragmentation was the introduction of four simple shape parameters – circularity, compactness, rectangularity, and elongation – to fully describe particle morphology [22]. Further reduction to two compound SPs showed that ash particles generated by different inferred fragmentation processes – such as 'dry' magmatic vs. hydromagmatic eruption styles [22,75] or ductile vs. brittle mechanisms [10] – defined specific 'fields'. These diagnostic fields have been widely applied to infer the origin of ash deposits (e.g. [39,59,60]), although the extent to which these shape parameter thresholds are translatable between deposits of different grain size, textural or compositional characteristics has not been addressed.

The question of generality versus uniqueness highlights another fundamental consideration in shape analysis: how best to interpret morphological data. Although process is often inferred from absolute values of measured SPs (e.g., [10]), morphological data may also be compared to other measured ash properties – such as the bubble number density or size distribution – to answer specific questions of fragmentation [49,57] or particle settling [1,52,69]. Increasingly, statistical tests, such as t-tests and equivalence tests, are being used to interpret particle shape data. For example, statistical comparison of SPs measured for both natural hydromagmatic ash and the experimental products of fragmentation experiments has been used to highlight the role of pre-stresses in shaping the fine ash produced during hydromagmatic eruptions [25,39]. Fractal analysis has also been used to explore the extent to which particles produced by different fragmentation mechanisms [51,56,62,63,68,74], or affected by different transport processes [12], can be distinguished based on the fractal properties of the particle perimeter. For example, using ash samples from a range of eruption styles, Maria and Carey [51] demonstrated that fractal spectra could be reduced to two principle components defined by coarse-scale and fine-scale perimeter complexity. As principal components are derived measures, however, it is difficult to uniquely ascribe differences to specific morphological features [51].

The need for rapid methods of data acquisition that can be used for volcano monitoring and surveillance is driving new research on methods of rapid particle characterisation [47,56,77]. Optical particle

analysers (OPAs) now enable size and shape analysis of large numbers of particles (10^2 – 10^4) on timescales of minutes to hours. Critically, assessment and application of data obtained from these methods has not yet been fully developed.

Although most SP studies have analysed 2-D representations of particle shape (either thin section analysis or projected view), the importance of characterising shape in three dimensions is becoming increasingly recognised for questions relating to particle settling. Particles often tumble as they fall and thus all possible projections contribute to the overall particle drag [92]. Inferring 3-D morphology from 2-D images requires the particle morphology to be homogeneous in all orientations [4,8,23]. Shape corrections for particle drag are typically formulated using 3-D parameters (e.g., sphericity; [21,23,24,29]). The 3-D equivalent of 2-D shape parameters can be estimated by averaging measurements from images taken from multiple viewing angles [21,23] or from multiple cross-sectional cuts [68]. New techniques, such as laser scanning and computed tomography, enable direct measurements of particle shape in three-dimensions (e.g. [4,85]), and SEM micro-CT techniques are capable of resolving features ∼3.5 μm in diameter [85]. At present, however, the additional acquisition and processing complexities (e.g., cost, acquisition and processing time, instrumental limitations) of these methods limit analysis to a small number of individual grains. For this reason, we therefore consider only 2-D shape parameters, which can be measured easily on statistically significant sample sizes.

2.3. Reference datasets used in this study

The wide range of morphologies exhibited by volcanic ash particles, often within a single sample, provides exceptional reference datasets with which to test the efficacy of different shape parameters. We use as a reference cross-sectional (2-D) images of glassy juvenile ash particles from Maria and Carey [51] that derive from a number of different volcanic environments, including submarine, shallow water (mafic), and dry subaerial (silicic). These environments are characterised by very different eruptive styles, each involving a different mechanism of magma fragmentation, and therefore provide a useful reference dataset to describe the *range* of possible ash shapes. Using these images, we calculate multiple shape parameters for each particle (using the shape analysis macro for ImageJ provided in the online supplementary material). Importantly, all particles are from a single sieve size fraction 250–500 μm (1–2φ).

For sensitivity analysis, we use 2-D (BSE–SEM) images of volcanic ash from two Icelandic eruptions: 2010 Eyjafjallajökull (EY2010) and 2011 Grímsvötn (G2011; [48,49]). G2011 samples were collected at distances of 60 and 115 km from the vent on 22 May 2011 (samples G6 and G1, respectively; [61]); the ash produced by this eruption comprises sparse microlites in a glassy (and bubbly) matrix (Fig. A1, supplementary information; [49]). The EY2010 ash sample (EY1) was collected during the first explosive phase of the summit eruption on 15 April 2010, from a location approximately 50 km from the vent [31]. In contrast to G2011, ash particles are heterogeneous in overall crystallinity, crystal texture and vesicle content (Fig. A1, supplementary information; [18,48]). Juvenile ash particles from both EY2010 and G2011 have previously been classified into different ash 'components', based on both their external morphology and internal bubble/crystal textures [18,49], and thus provide useful datasets to optimise SPs to describe variable ash particle morphologies.

3. Optimising shape parameter selection

Individual SPs represent non-unique descriptions, such that it is impossible to reconstruct the original particle shape based on the value of a single parameter (e.g. [32]). Although this inverse problem

can be better constrained by using multiple parameters, each sensitive to a different aspect of particle morphology, the optimal number of shape parameters to include must be determined: use too few and the particle shape will be insufficiently constrained, use too many and the volume of data will be computationally inefficient. Here we use multivariate statistics to explore the relationships between SPs and identify the (minimum number of) parameters most appropriate for volcanic ash characterisation.

3.1. Shape parameter categories

The overall irregularity of particle shape depends on both form and roughness, each of which can vary independently. Surface roughness, additionally, occurs on a range of scales (relative to the particle size) and includes both perimeter-based (textural) and area-based (morphological) roughness. Simple SPs (Table 2) are typically sensitive to one of these specific morphological properties; below we group these commonly-used SPs by their morphological sensitivity. Compound parameters, such as the concavity index (Table 2; [49]), comprise multiple simple SPs and therefore combine information from different aspects of morphology.

Morphological roughness: solidity (SLD), compactness (CP), defect area (DeltA), and extent (EXT) quantify the spatial distribution of particle area, and as such are most sensitive to particle-scale concavities. All compare particle area to the area of a bounding reference shape, typically either a bounding rectangle or a convex hull (Fig. 2).

Textural roughness: convexity (CVX), rectangularity (RT), Paris factor (PF), and CVX_feret (CVX_f) represent perimeter-based measures of surface roughness, again compared to a bounding reference shape. They are most sensitive to small-scale concavities (relative to the particle dimensions) that increase the particle perimeter.

Form: Axial ratio (AxlR), elongation (EL), aspect ratio (AR), and roundness (RD) measure the relative difference between two particle dimensions, although parameters differ in how the particle dimensions are defined. For example, the 'axial' ratio compares the minor to major axes of the best fit ellipse, whilst the 'aspect' ratio compares the minimum and maximum particle Feret diameters (Table 2).

3.2. Using cluster analysis to explore the relationships between shape parameters

Cluster analysis and cladistics assign 'objects' to groups (also referred to as clades or clusters) based on the similarity of objects. Importantly, no *a priori* assumptions regarding the underlying distribution are required. The objects are usually a series of physical entities, each defined by a number of discrete or continuous variables. Cladistics and cluster analysis are suited to the analysis of discrete and continuous variables, respectively [38]. Cladistics is used extensively in evolutionary biology to explore phylogenetic relationships amongst species, and to identify shared derived characteristics amongst monophyletic groups (e.g. [55]). Discretisation of continuous variables into discrete character states, however, introduces artificial divisions such that small differences in a particular character may be overemphasised [16,64]. The input matrix for cluster analysis, in contrast, uses continuous variables and takes the form of a distance measure, such as the Euclidean distance (i.e., the geometric distance between two objects in multi-dimensional space).

Shape parameters are continuous variables, so we can use cluster analysis to determine the minimum number of SPs needed to characterise morphology. By inverting the traditional clustering approach to make the properties themselves (the SPs) the subject of the analysis, we highlight the relationships between different parameters measured on the same particle population [32]. A clustergram is the visual output of cluster analysis, and groups variables according to their

degree of relatedness. Agglomerative clustering algorithms group the most related variables first, and then progressively reduce the number of clusters at each hierarchical level from n clusters of size 1, to one cluster incorporating all observations (i.e. a tree structure). The Ward method of minimum variance creates clusters at each step that minimise the increase in the error sum of the squares [89], and is the approach adopted in this study.

We apply cluster analysis to the simple shape parameters listed in Section 3.1 and measured on the reference images from Maria and Carey [51]. SPs divide into two main clusters that separate those sensitive to form/elongation from those measuring surface roughness (Fig. 3). Roughness parameters can then be further sub-divided into perimeter-based (textural roughness; blue box in Fig. 3) and area-based (morphological roughness; red box) measures. The result is not affected by removing a parameter, changing the order in which the parameters are arranged in the input matrix, or using an alternative clustering method (e.g., single 'nearest neighbour' clustering instead of the Ward method). Moreover, despite contrasting ash morphologies, the clustergram structures are very similar for all three reference datasets, showing that the relationships between simple shape parameters are largely independent of the morphology of the particles on which they are measured (in this case, ash generated by contrasting fragmentation styles). The exception is form factor (and its unbounded inverse circularity), which do not consistently appear in the same cluster.
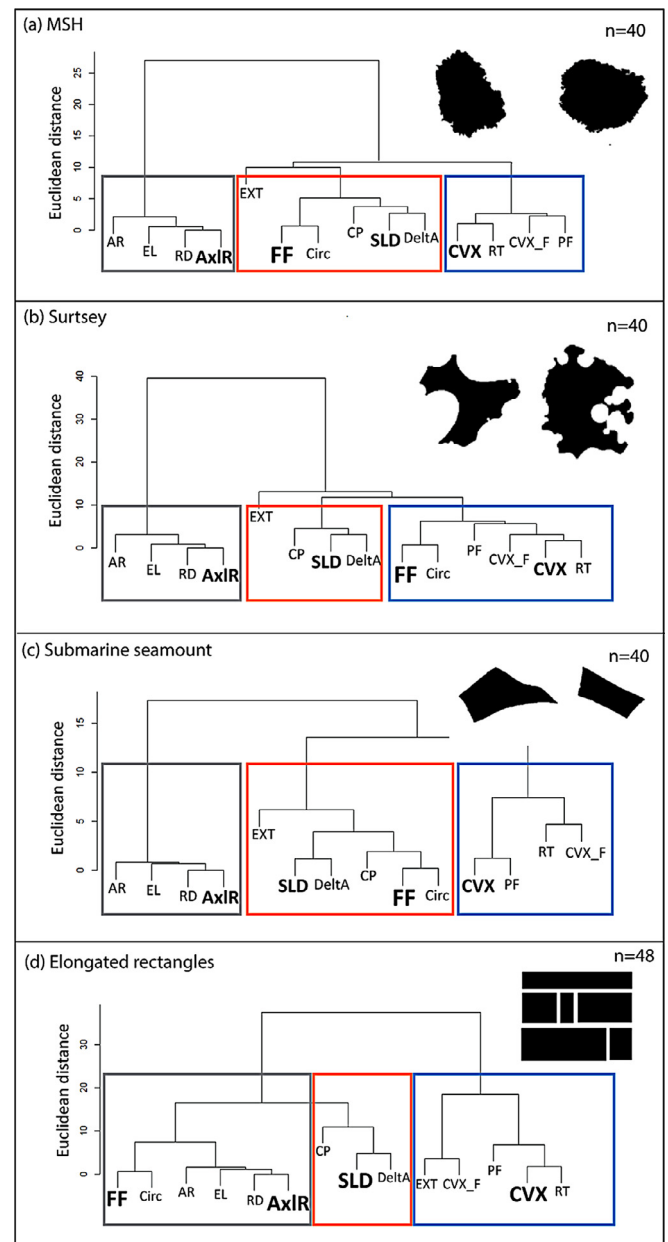
3.3. Shape parameter selection

The tri-modal structure of the clustergrams in Fig. 3 supports the categorisation described in Section 3.1, whereby parameters sensitive to textural roughness, morphological roughness, and form/elongation each cluster together. A three-parameter shape description, including one parameter from each of the three clusters, therefore provides an effective description of particle morphology. All parameters within a given cluster measure similar features of particle shape, albeit in subtly different ways; therefore including more than one shape parameter from a single cluster would yield no appreciable additional information, and adds further computational complexity. Furthermore, using only one parameter from each cluster ensures that the overall shape description comprises shape parameters that behave largely independently of each other, and is not biased towards any particular aspect of morphology.

Form factor (FF) and circularity (Circ) are two exceptions, as illustrated by their variable placement in the clustergrams. These two parameters measure the deviation of a particle from a circle, which can result from either changing particle elongation or increasing surface roughness. Hence, these parameters will group with whichever feature of particle morphology is causing the particle shape to deviate from the reference. For example, if the main difference between particles is the particle-scale concavity of their outlines, then FF and Circ will resemble measures of morphological roughness such as solidity (e.g., Fig. 3a and c). If small-scale complexity in the particle outline is instead the main distinguishing feature, then FF and Circ will group with textural roughness parameters such as convexity (e.g., Fig. 3b). By this reasoning, for particles of similar roughness but variable elongation, FF and Circ should group with form/elongation parameters, as shown by a population of elongated rectangles (Fig. 3d).

In summary, we have demonstrated through cluster analysis that three shape parameters (one from each of the three clusters shown in Fig. 3) are needed to provide the minimum robust shape description. Cluster analysis does not, however, provide any indication of which parameter should be selected from within each cluster. We therefore assess the suitability of each parameter using criteria based on the considerations identified in Section 2.1:

(1) Are the parameters scaled equally?

Fig. 3. Identifying the optimal shape parameters. Cluster analysis of shape parameters from re-analysis of particle images [51] for (a) 1980 Mt St Helens MSH (fall deposits only) and (b) 1963–64 Surtsey, Iceland, and (c) a submarine seamount. Form factor (FF), solidity (SLD), convexity (CVX), and axial ratio (AxlR) are shown in bold for clarity. The boxes delimit the three clusters of shape parameters sensitive to particle elongation (grey), area-based roughness (orange), and perimeter-based roughness (blue). Inset images show representative examples of ash particles from each sample. (d) Cluster analysis of shape parameters measured on an image containing rectangles of different dimensions. (For interpretation of the references to colour in this figure legend, the reader is referred to the web version of this article.)

(2) Is the reference shape appropriate?
(3) Is the measurement independent of the image used?

Circularity, elongation, rectangularity and compactness are most commonly used to characterise volcanic ash [10,17,22,39,58,60,75], and are indeed distributed across the three clusters in Fig. 3. However, these four parameters include both scaled and unscaled parameters, such that equal weight is not given to each measurement in discrimination diagrams. Furthermore, rectangularity and compactness both use the bounding box as a reference shape, which is not only dependent on 2-D particle orientation (as it uses an X–Y Cartesian

reference frame; Section 2.1), but also does not represent the fully compact form for irregularly-shaped ash particles. Instead, we recommend the use of solidity, convexity, and axial ratio (SLD, CVX, and AxlR) as they are (a) equivalently scaled to the range 0–1, where a circle has a value of 1, and (b) normalised to the convex hull reference shape (SLD and CVX), which is entirely independent of particle form and orientation. For volcanic ash, the convex hull is a more appropriate reference shape than the bounding box (Fig. 2), as, in general, particles are not simple geometric shapes and roughness is in the form of vesicle concavities (e.g. [49,68]). The sensitivity of form factor (FF) to both elongation and roughness make it the best single parameter by which to assess overall irregularity. However, this co-dependence also makes FF non-unique in its physical interpretation, such that it provides few constraints on *how* the particle differs from a circular form. Although FF is equivalent to $(1/Circ)^2$, expressing the definition in this way ensures that FF is scaled consistently with other SPs (i.e., 0–1), and is a more sensitive parameter to small deviations from a circle. Our preferred SPs are the same four parameters used by Cioni et al. [18] and Leibrandt and Le Pennec [47], although neither study provides a rationale for their choice.

4. Data collection—how to acquire the most accurate images for shape analysis

Having identified the most useful shape parameters, we now consider how to measure them most accurately. Digital images provide the raw materials for shape analysis, and the accuracy of shape measurements is determined largely by the methodological decisions made during sample imaging [47]. We begin by describing each stage of the data collection process – from sample preparation through to image acquisition and processing – and review the different techniques available for particle imaging. Using our reference ash samples from G2011 and EY2010, we then assess the sensitivity of our recommended shape parameters – solidity (SLD), convexity (CVX), axial ratio (AxlR), and form factor (FF) – to the choice of imaging instrument (Section 4.1), the image resolution (Section 4.2), and the sample size analysed (Section 4.3). All shape data shown here are available from the University of Bristol's data repository [DOI: 10.5523/bris.765l15d6gbsj1vty17u2a8ky2].

4.1. Sample preparation and imaging

Ash samples were cleaned in an ultrasonic bath for 3–5 mins and dried overnight in an oven at 80°C. Dried samples were separated into discrete sieve size fractions ($<3\varphi$, 3.5φ, 4φ, 5φ, and $>5\varphi$, corresponding to >125 μm, 91–125 μm, 63–91 μm, 32–63 μm, and <32 μm respectively) prior to analysis. The reasons for this separation are two-fold: (1) image analysis is easier if the range of particle sizes is relatively uniform, as this ensures that all grains are imaged

at an equivalent resolution and remain in focus at a single magnification, and (2) pre-separation of different particle size populations enables morphological comparison between grain size fractions, and between samples with different grain size distributions (e.g. [49]). We quantify the particle shape characteristics of each size fraction using images obtained by three contrasting acquisition techniques: the Malvern Morphologi® G3 Particle Characterisation System (hereafter referred to as the optical particle analyser or OPA) and the Scanning Electron Microscope (SEM) operating in both backscattered electron (BSE) and scanning electron (SE) modes (Fig. 4).

4.1.1. Scanning electron microscope (SEM)

Separate sieved size fractions were mounted in carbon-coated polished grain mounts and analysed at the University of Bristol using a Hitachi S-3500N scanning electron microscope (SEM) operating in backscattered electron (BSE) mode (Fig. 4a). Sub-samples of the same size fractions were also mounted on carbon stubs and gold-coated for imaging in secondary electron (SE) mode (Fig. 4b). Automated grid images were acquired for each sample size fraction using a working distance of ~18.0 mm ($z = 20$ mm) and either a 20 kV (SE) or 15 kV (BSE) accelerating voltage. Each grid image comprises manually stitched collages of 20–40 images, and contain between 1158 and 2974 particles. Optimising the acquisition magnification for each grain size fraction ensured that the image resolution was independent of grain size (see Section 4.3). Grid images were acquired at a resolution of 2.56 to 0.29 pixels/μm for grain size fractions of $<3\varphi$ to $>5\varphi$ (>125 μm to <32 μm), respectively, yielding an average pixel density over all size fractions of 2211 pixels per particle (pxl/p). Re-imaging at a higher resolution (average pixel density of ~20,000 pxl/p) and over a larger number of images (up to 81 images per grid) did not yield significantly different results, and offered little advantage for the additional computational expense.

Particle overlap was negligible in BSE images due to effective grain separation in the polished mounts. However, overlap contributed a source of error to analysis of SE grid images, which required some manual particle separation. Complications associated with aggregation and overlap are more significant when working with the smaller size fractions due to greater cohesive forces between particles.

All subsequent 2-D shape analysis was performed using the ImageJ image analysis software (http://imagej.nih.gov/ij/). Images were thresholded to binary and filtered using noise reduction to eliminate one-pixel outliers, followed by a single 'close' operation (pixel dilation, followed by erosion). This filtering combination minimised artificial complexity added to the particle outline during thresholding, whilst preserving the original particle shape. Raw particle size measurements of all grains (excluding edge-intersecting particles) included area (including internal holes), perimeter, major and minor axes of best-fit ellipse, width and height of bounding rectangle, maximum and minimum Feret diameters, convex hull area
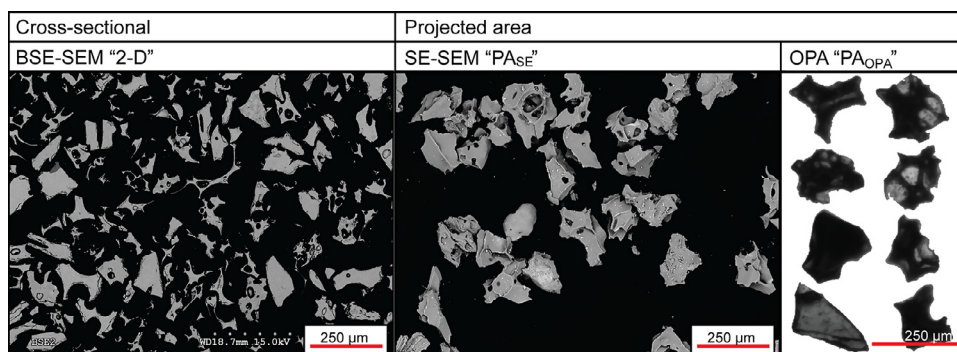

Fig. 4. Methods of particle imaging. (a) Backscattered electron scanning electron microscopy "2-D" (or BSE–SEM). (b) Secondary electron scanning electron microscopy "PA$_{SE}$" (or SE–SEM), and (c) optical particle analyser "PA$_{OPA}$".

and convex hull perimeter (Table 1). These primary measurements were then used to calculate the 2-D shape parameters listed in Table 2. The macro for ImageJ used for all shape measurements has been made available in the online supplementary material.

4.1.2. 'Morphologi' optical particle analyser

The 'Morphologi' optical particle analyser (OPA) offers rapid automated analysis of a statistically significant number of particles (10^3–10^5 per scan). Each analysis requires only a small sample volume (10–20 mm^3), which is then retrievable. Samples are dispersed onto a glass slide using compressed air within an automated dispersing unit. A digital microscope acquires separate images of each particle under diascopic light according to various parameters (e.g., optical magnification, threshold, and scan area) that are specified by the user. As the grain size of the sample decreases, the number of particles per unit area increases significantly; the total scan area is therefore progressively reduced with decreasing grain size to prevent unnecessarily long acquisition times. More detailed methodological descriptions and recommended protocols for the OPA are presented in Leibrandt and Le Pennec [47].

Particle outlines are defined based on a specified grain-to-background contrast ratio, or threshold (Fig. 4c). Incorrect threshold selection can introduce errors: a threshold set too low may not detect very thin regions of the particle (yielding a pixelated outline and high textural roughness values), whilst too high a threshold may include portions of the background as part of a grain (thereby increasing both area and apparent roundness). It is impossible to define a single threshold value appropriate to all particles, therefore some degree of filtering is necessary. The automated sample dispersion unit minimises particle overlap, although manual filtering is required to remove particle clusters, especially for smaller size fractions.

Commercial and publicly-available software use different conventions to measure particle properties. For example, ImageJ calculates particle perimeters by measuring the total boundary length of the region of interest (http://imagej.nih.gov/ij/); Malvern Morphologi® software, in contrast, determines perimeter (L) by weighting each edge pixel according to whether it is part of a straight line, a sloped line or a corner [86]:

$$L = (0.980 \times E_t) + (1.406 \times E_s) - (0.091 \times C_n), \qquad (1)$$

where E_t, E_s, and C_n refer to straight-edge, sloped-edge, and corner pixels, respectively. The two programs also differ in their measurement of particle dimensions. ImageJ defines the aspect ratio (herein referred to as axial ratio) as the ratio of the major and minor axes of the best-fit Legendre ellipse (by default). In Malvern software, however, aspect ratio refers to the ratio of the longest distance between any two points on the perimeter projected onto the major (length) and minor (width) rotation axes (Malvern Instruments Ltd., 2010).

4.2. Cross-sectional versus projected images

Image acquisition techniques generally belong to one of two categories depending on whether images comprise cross-sectional (2-D slices) or projected areas (PAs). For example, whilst shape analysis using BSE–SEM images obtained from a thin section or polished grain mounts provide true cross-sections, OPAs and SE–SEM image projected area. To evaluate the influence of image acquisition methods on shape analysis, we directly compare shape data for our four recommended parameters – FF, CVX, SLD, AxlR – obtained for the same ash samples (and size fraction) by the three methods (BSE–SEM ["2-D"], SE–SEM ["PA$_{SE}$"], and Morphologi OPA ["PA$_{OPA}$"]).

The histograms and cumulative shape data obtained from the three different imaging techniques are shown in Fig. 4 (G2011; G6 4φ) and supplementary Fig. A2 (EY2010; EY1 4φ). Here it is clear that the SP distributions based on PAs are consistently shifted towards higher values (i.e., more closely approximating a circle [FF] or convex form

[CVX, SLD]) than the equivalent cross-sectional distributions. However, individual SPs show different sensitivities to image acquisition technique. FF measurements show the greatest discrepancy between 2-D and PA images: whilst measurements on 2-D images yield a left-skewed distribution with a modal value of 0.25, both PA$_{OPA}$ and PA$_{SE}$ distributions are right-skewed and have modal values of 0.55 and 0.65, respectively (Fig. 5a and b). The distributions of SLD and CVX are similar, and are strongly right-skewed regardless of the acquisition method. However, whilst measurements from PA$_{OPA}$ and PA$_{SE}$ have a narrow range of values close to 1 (i.e., very little deviation from a fully convex form), 2-D images have a much broader range (0.2–0.9 for SLD and 0.45–1.0 for CVX). AxlR measurements are approximately normally distributed for all three methods, but again the modal value is considerably lower for 2-D images (0.5) compared to those of projected area (0.65–0.7; Fig. 5d and e).

To summarise, 2-D (cross-sectional) images typically yield shape parameter distributions that are skewed towards low values; that is, measurements are more elongated, and exhibit much greater variability in surface roughness/irregularity, than those obtained from PA images of equivalent particles. This difference is easily explained by the smoothing effect of projecting a 3-D particle onto a plane, and is amplified for FF due to its co-dependence on elongation and roughness.
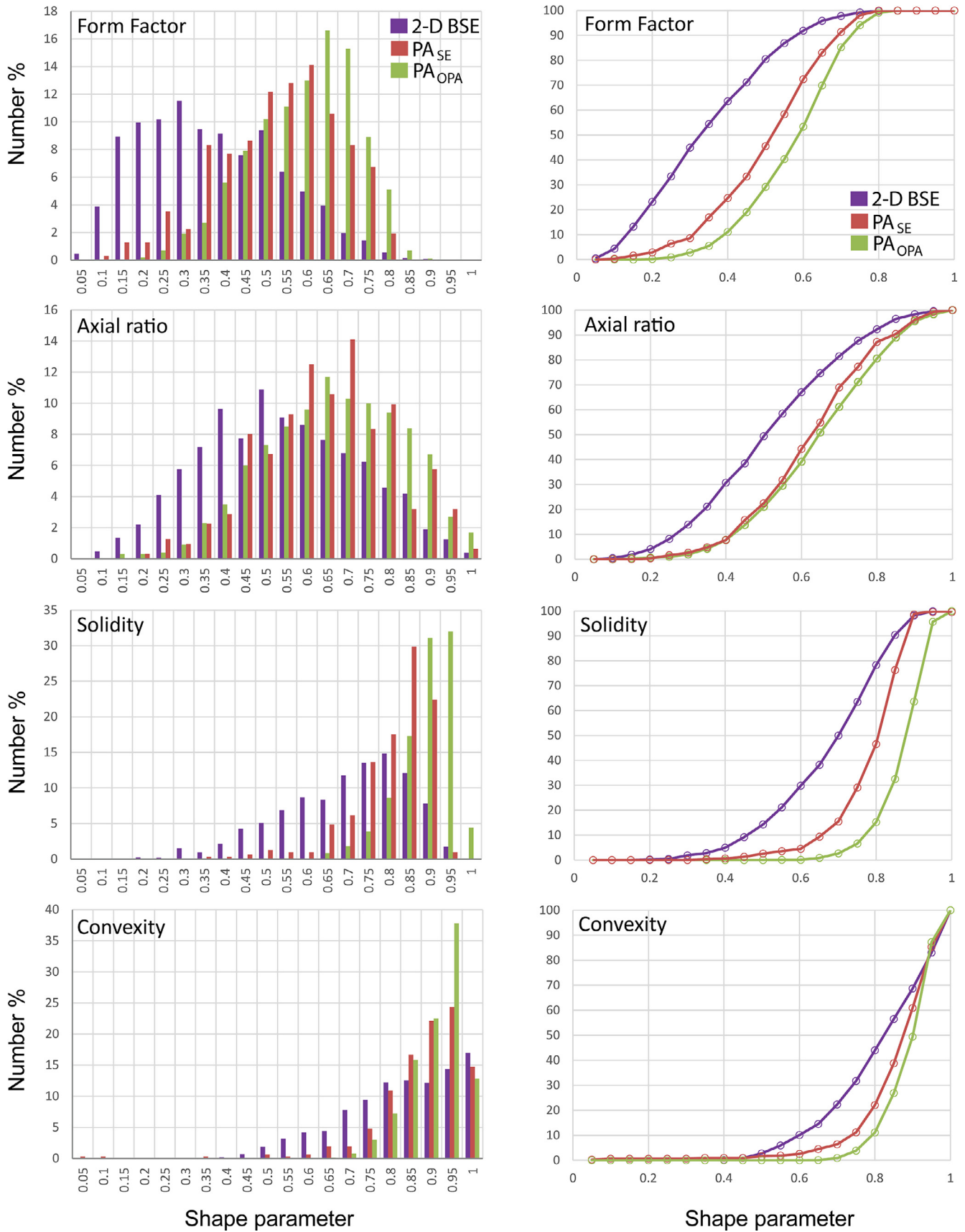
More surprisingly, the two acquisition methods that obtain images of projected area do not yield identical shape parameter distributions. Images obtained using the OPA consistently suggest smoother and more convex particles, although the shape distributions for AxlR are comparable between the two methods. These differences are not a consequence of the software, as we exported the PA$_{OPA}$ images for analysis in ImageJ. Alternative sources of discrepancy include subtle differences in either the subsample selected for mounting or the orientation of the grains due to mounting on adhesive (PA$_{OPA}$) vs. non-adhesive surfaces (PA$_{SE}$). Nevertheless, differences in shape as a function of orientation are most apparent for flat or elongated particles, so we would expect an adhesive surface to record a greater range of AxlR measurements, contrary to what is observed (Fig. 5). Instead, the offsets in FF, SLD, and CVX are most likely related to the difficulty in keeping all parts of a 3-D particle outline in sharp focus when using optical imaging techniques. Blurring of some, or all, of the outline would increase the apparent smoothness (and compactness) of the particle, with little effect on the elongation. The use of smaller particle size ranges, such as ¼φ size classes, may help to maintain optical focus when imaging with OPAs [47].
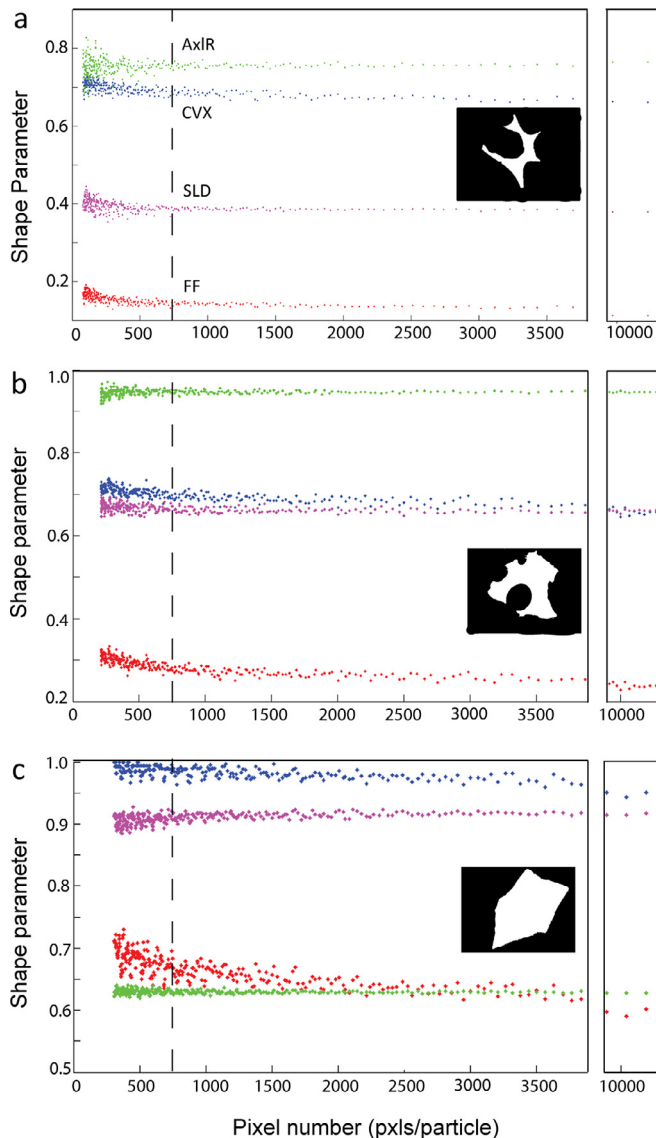
4.3. Image resolution

The number of pixels comprising a particle image can strongly influence the apparent morphology, and hence the corresponding SPs. This is particularly true for measurements of perimeter where the pixel density (pxl/p) determines the level of detail. Comparative shape analysis therefore requires a constant pixel density between particle images, or between particles within an image [22,32,83,72]. Pixel density for a given particle size (and working distance) is a function of the image magnification and resolution. A constant pixel density of ~5000 pxl/p has been recommended by several authors [23–25,52], although no explicit justification has been given for choosing this threshold.

To quantify the influence of resolution on different shape parameters, we measured our four preferred shape parameters – FF, CVX, SLD, and AxlR – on three BSE–SEM images of ash grains (100–120 μm) with contrasting morphologies: a dense blocky fragment, a moderately vesicular particle, and a concave glass shard (from G2011; [49]). Each image was acquired at a resolution of 2560 × 1920 pixels (corresponding to >10^6 pxls/p), then systematically subsampled to yield pixel densities of 10^1–10^6 pxls/p (Fig. 6). Reducing the pixel density causes SPs sensitive to surface roughness (FF, CVX) to
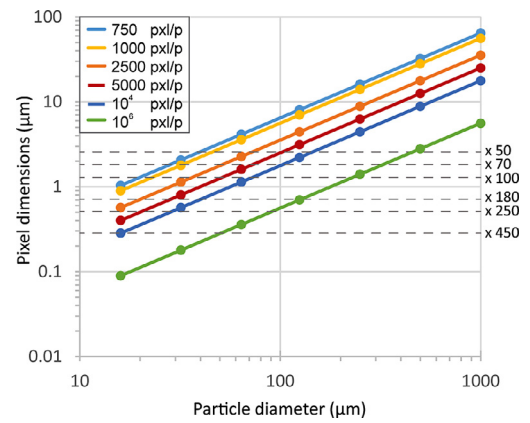
Fig. 5. The influence of the image acquisition method on shape measurements. Number distributions of (a) form factor, (b) axial ratio, (c) solidity and (d) convexity, measured on 2-D (purple), PA_{SE} (red) and PA_{OPA} (green) images of ash particles from the 4φ size fraction of G2011 G6. (For interpretation of the references to colour in this figure legend, the reader is referred to the web version of this article.)

Fig. 7. Minimum pixel dimensions required for different pixel densities, as a function of particle size. The dashed horizontal lines show how pixel dimension varies with BSE–SEM magnification, for a working distance of ∼18 mm ($z = 20$ mm) and standard image resolution of 1024 × 960.

particle shape. Fig. 7 was calculated for the simplest case of a circle; as the particle outline becomes more complex, a higher magnification is required to achieve the same number of pixels per particle.

4.4. Sample size

The number of particles needed to characterise the range of shapes within a population is a balance between sample statistics, acquisition time, and data file size. OPAs can image 10^3–10^5 grains, a considerable advantage over conventional SEM-based methods, which not only involve considerably more sample preparation, but also yield fewer particle measurements for reasonable acquisition times and manageable file sizes (typically 10^3 particles per sample). A recent study by Leibrandt and Le Pennec [47] demonstrated that average values of AR, CVX and Circ converge to stable values (relative standard deviation, RSD <0.2%) for sample sizes >150 grains at 1φ (500 μm), >700 grains at 2φ (250 μm) and >1000–2000 grains at 4φ (63 μm). Using a similar approach for PA$_{OPA}$ measurements of G2011 ash samples (4φ), we obtained comparable results for FF, CVX, SLD, and AxlR, whereby average values stabilise for counts of 1000–2000 grains (Fig. A3, supplementary information). These critical sample sizes of 150–2000 grains (depending on the grain size) are also easily achievable by SEM methods, validating that shape measurements from SEM images are statistically robust.

The sensitivity studies described in Sections 4.1–4.4 demonstrate that the choices made during the image acquisition stage have consequential effects for the accuracy of the resulting shape measurements. We summarise the preceding discussion and outline our preferred methodology (including sample preparation, image acquisition, and shape parameter selection) in the supplementary information (Appendix A). For research questions related to fragmentation, we favour 2-D SEM images over OPA images of projected particle area as (a) it is easier to maintain optical focus, resulting in sharper particle outlines, (b) 3-D morphological features are not superimposed, and (c) particle shapes can be directly compared to their corresponding internal crystal and bubble textures. Nevertheless, alternative applications of shape analysis will have different requirements; for example, the low cost per analysis and short acquisition times achievable with OPAs are advantageous for volcano monitoring purposes [47]. In the following sections, we demonstrate how shape measurements from 2-D SEM images can be used to address specific volcanological questions. We focus particularly on how differences in measured shape parameters translate to physical properties, and therefore how morphological datasets can be used to test hypotheses related to particle formation.

Fig. 6. Sensitivity of shape parameters to image resolution, showing the variation in calculated form factor (red), solidity (purple), convexity (blue) and axial ratio (green) for single particles that are progressively subsampled. (Insets) particle images used in each sensitivity study. The vertical dashed line highlights the critical pixel density of 750 pxls/p, below which the scatter in shape parameter values increases considerably. (For interpretation of the references to colour in this figure legend, the reader is referred to the web version of this article.)

increase towards a value of 1 (i.e., the particle appears progressively smoother). AxlR, in contrast, may either increase or decrease (particularly for highly irregular bubble shards) and FF and CVX vary continuously as pixel density is reduced. Importantly, FF and CVX contain a perimeter term in their definitions, from which detail is lost most rapidly with progressive subsampling. As the pixel density is reduced from ∼10^6 to 10^2 pxls/p, FF and CVX can increase by a factor of 2–3 depending on the particle morphology (Fig. 6). AxlR and SLD, in contrast, remain stable until reaching a critical pixel density of ∼750 pxls/p.

We conclude that a minimum critical pixel density of 750 pxls/p is required for robust assessment of AxlR and SLD. In contrast, FF and CVX can only be directly compared when image magnification during acquisition is optimised to ensure that the images are scale-invariant. The minimum pixel dimensions required to achieve specific pixel densities for each grain size fraction (assuming equivalent diameter circles) are shown in Fig. 7. An additional consideration is the

5. Interpreting shape data in the context of volcanic ash properties
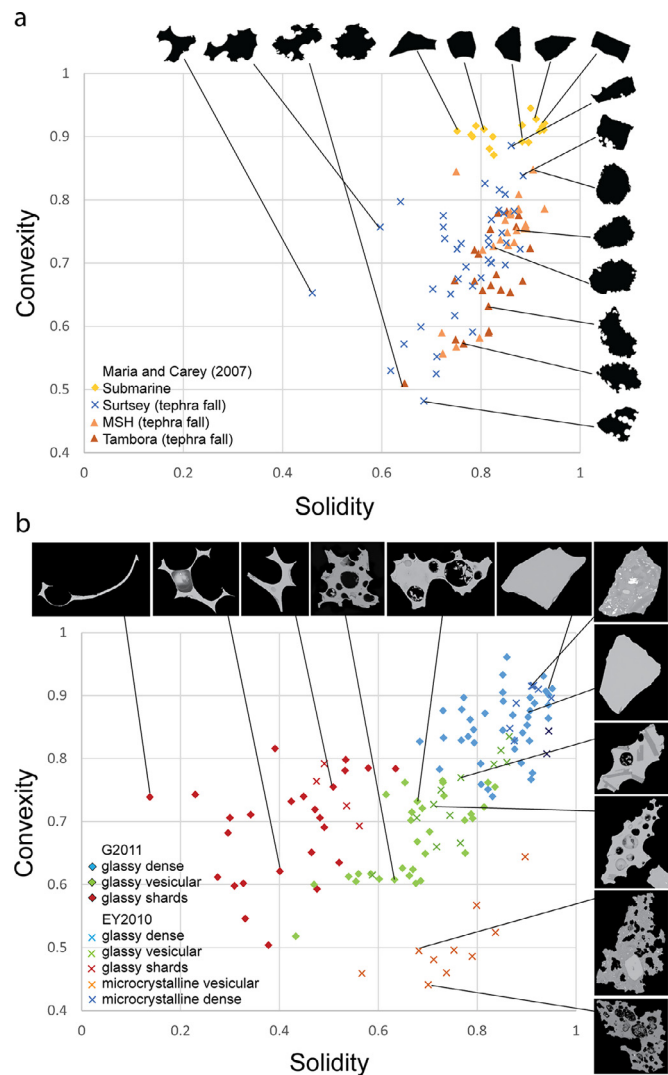
5.1. Developing discrimination diagrams

The goal of most particle shape studies is to classify particles into different morphological types, or 'components'. In volcanology, ash components are typically defined by aspect ratio, the presence or absence of angular vertices (from brittle breakage), and the size/abundance of vesicles that define the particle outline. Several discrimination diagrams have been proposed to distinguish between the products of brittle and ductile fragmentation [10] or magmatic and hydromagmatic fragmentation [58,75]. These diagrams reduce four SPs – circularity, elongation, rectangularity and compactness – to two compound parameters that define the axes. An alternative diagram uses the concavity index (CI; a compound parameter combining CVX and SLD) to differentiate between dense fragments and bubbly grains (vesicular particles and bubble shards; [49]). Combining simple SPs into compound parameters maximises the information that can be presented on a two-axis plot, but at the expense of morphological information.

For a given particle population, clustergrams (Figs. 3 and A1) can be used to assess which simple SPs will best define the range of particle shapes. As discussed in Section 3.3, form factor (FF) will group with whichever feature of particle morphology is causing the particle shape to deviate from a circle. Accordingly, the position of FF on a clustergram provides a preliminary indication of which SPs are likely to dominate the variance for a given population, and are therefore likely to be useful in the design of an effective discrimination diagram. We outline this concept using our two reference datasets of 2-D ash particle images (Section 2.3):

Example 1. The clustergrams for the reference samples of Maria and Carey [[51]; Fig. 3] show that form factor (FF) moves between the textural and morphological roughness clusters. This behaviour suggests that shape parameters such as convexity (CVX) and solidity (SLD) dominate the variance within these samples, and that axial ratio (AxlR) contributes little to the morphological variation. CVX is essentially a measure of the 'excess perimeter' of a particle relative to that of its convex hull (textural roughness), whilst SLD measures the difference in area between a particle and its fully convex form (morphological roughness). A plot of SLD vs. CVX (hereafter referred to as a SLD–CVX diagram), can therefore be used to differentiate the influence of particle-scale concavities from that of small-scale irregularities in controlling overall roughness (Fig. 8a).
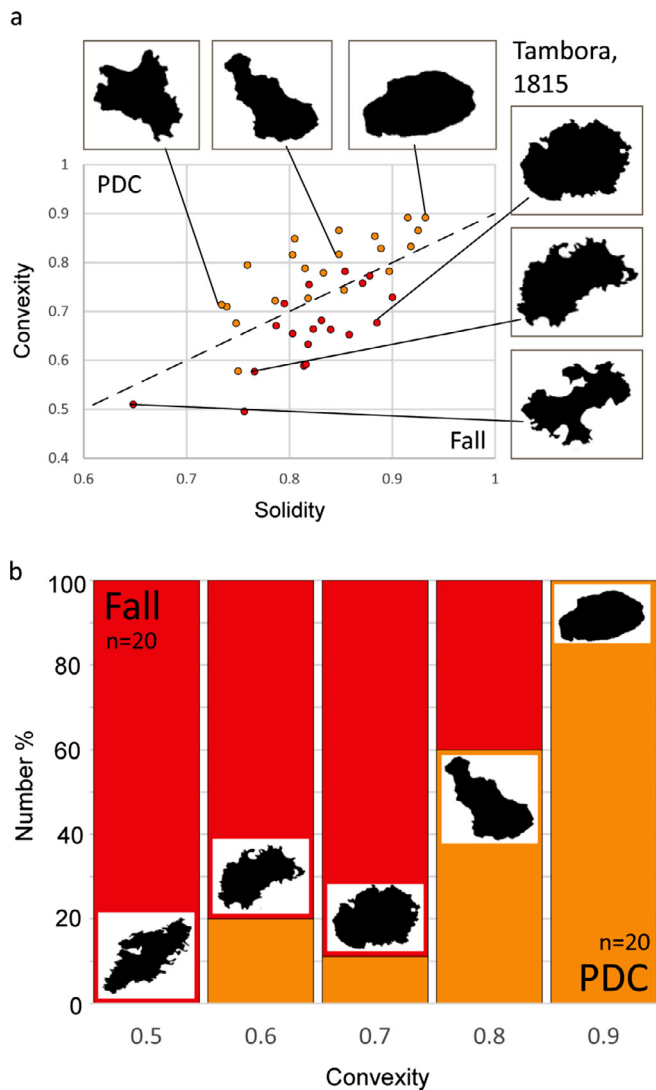
Firstly, it is clear from Fig. 8a that submarine (vesicle-free) fragments form a distinct morphological cluster. These dense ash particles are characterised by smooth, straight-edged outlines with little perimeter concavity, which translate to high values of convexity (CVX > 0.85) and solidity (SLD > 0.75). In comparison, vesicular ash particles from the eruptions of MSH, Tambora and Surtsey typically share lower values of convexity (0.5 < CVX < 0.85), but retain a similar range in solidity. Physically, this reflects the introduction of perimeter-intersecting concavities, where the indentation size (i.e., vesicles) is much smaller than the particle. The shapes of ash particles from the hydromagmatic Surtsey eruption are not significantly distinct from those produced by subaerial magmatic fragmentation (MSH and Tambora) in the studied size range, but do extend to lower solidities (0.45 < SLD < 0.9) for the most concave forms. Importantly, the main *quantifiable* morphological distinction in this example is between dense and bubbly particles, which can be determined from convexity measurements. For this range of particle sizes (250–500 μm), solidity varies over a relatively restricted range of values and is therefore of limited use as a discriminator.

Interrogating the data in more detail, it is possible to explore shape variations within individual populations. For example, the

Fig. 8. The relationship between particle shape and eruption style. Solidity vs. convexity (SLD–CVX) diagrams comparing (a) 250–500 μm (2φ) particles from different eruption styles, based on re-analysis of particle images from Maria and Carey [51]. At this particle size, the main difference in shape is between particles from submarine (dense) and subaerial (bubbly) eruptions; (b) different ash components from the 91–125 μm (3–3.5φ) size fraction of G2011 (diamonds; [49]) and EY2010 (crosses; [48]). Particles have been manually classified into the following component classes: dense fragments (blue), bubble shards (red), or vesicular. For EY2010, vesicular particles have been subdivided further into glassy (green) and microlite-rich (orange). As particle size begins to overlap the range of bubble sizes, it becomes possible to distinguish between bubble shards and vesicular particles using SLD. (For interpretation of the references to colour in this figure legend, the reader is referred to the web version of this article.)

reference dataset from Tambora includes glassy ash particles sampled from both fall and pyroclastic density current ('flow') deposits, and which exhibit different fractal properties [51]. Differentiating ash particles from each population on the SLD–CVX diagram (Fig. 9) shows that particles from flow deposits have elevated CVX values (with 90% of particles 0.7 < CVX < 0.9) compared to those emplaced by direct fallout (0.5 < CVX < 0.8). Ash from both deposits exhibits a similar range in solidity (with 90% of all particles 0.73 < CVX < 0.9; Fig. 9a). Expressed alternatively, the proportion of flow particles (relative to fall particles) as a fraction of the total number of grains within each convexity class increases almost linearly with increasing convexity (Fig. 9b). Assuming that fall deposits are representative of the initial ash morphology from primary fragmentation, this shift suggests smoothing of the fine-scale roughness during flow transport, without significantly altering irregularity at the particle-scale. Although

Fig. 9. Identifying transport processes using shape analysis. (a) Solidity vs. convexity (SLD–CVX) diagram comparing particles from fall and pyroclastic density current ('flow') deposits from 1815 eruption of Tambora (images from [51]). (b) Variation in the relative proportions of fall and flow particles as a function of convexity, expressed as a percentage of the total number of particles within each convexity class.

not intended to be a fully comprehensive analysis (for which sample sizes of $\geq 10^3$ particles and information on the componentry assemblage, including non-juvenile material, would be required), these preliminary results are consistent with gradual abrasion through low-intensity collisions, and therefore a dominance of comminution processes over disruption and brittle breakage in this example [26]. Fractal analysis of the same data set also suggests that particle-particle interaction decreased the fine-scale perimeter complexity of individual particles [51].

Example 2. The clustergrams for EY2010 and G2011 samples show that, again, the affinity of FF varies between SLD and CVX (Fig. A1, supplementary information), suggesting that same SLD–CVX discrimination diagram is likely to be useful. Each ash particle within these two datasets has been manually classified as belonging to one of five components – glassy dense, glassy vesicular, glassy shard, microcrystalline vesicular, or microcrystalline dense – based on their external morphology and internal crystal and bubble textures. Fig. 8b shows that ash particles belonging to each component occupy distinct fields of the SLD–CVX diagram, and that corresponding components from EY2010 and G2011 overlap. Dense, vesicle-poor
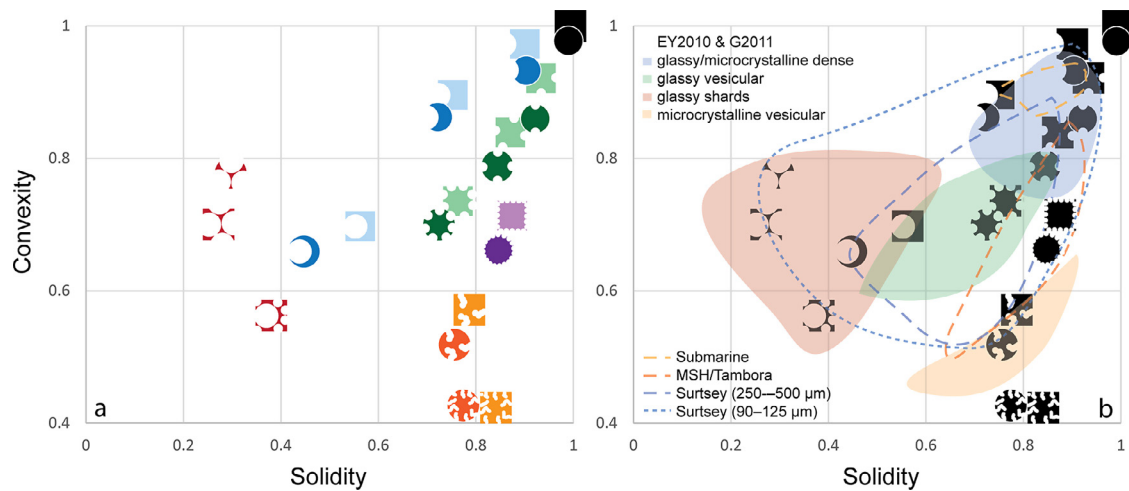
fragments (both glassy and microcrystalline; shown in blue) resemble 'submarine' glassy fragments from Fig. 8a, and accordingly have similar high values of solidity and convexity. 'Bubbly' grains of varying vesicularity (including glassy shards and glassy/microcrystalline vesicular particles) have consistently lower convexity values (CVX < 0.8), but, importantly, exhibit a much wider range of solidities (0.1 < SLD < 0.9). In detail, glassy shards comprise the lowest measured solidities (SLD < 0.6; shown in red), whilst vesicular grains – both glassy (green) and microcrystalline (orange) – are typically more compact (SLD > 0.6). Shards and vesicular particles can therefore be differentiated using solidity measurements, based on quantifiable differences in the size of concavities relative to the particle size. Lastly, microcrystalline vesicular particles form a distinctive cluster, characterised by very low convexity and high solidity (Fig. 8b). The presence of irregular, polylobate vesicles, which are often deformed around crystal boundaries, lengthens the particle perimeter considerably relative to the fully convex shape, whilst maintaining very compact forms.

Compared to the reference dataset in Fig. 8a, ash particles from the 91–125 μm size fraction of G2011 and EY2010 span a much broader range of shape parameter values. In particular, the range in solidity has more than doubled, reflecting greater variability in the size of perimeter-intersecting concavities relative to that of the particle. This is largely an effect of the difference in grain size class used between Fig. 8a and b, which will be explored further in Section 5.3. Whilst the range of particle sizes in the reference dataset from Maria and Carey [[51]; 1–2φ or 250–500 μm] are significantly larger than the size of constituent concavities (i.e., vesicles), the smaller particle sizes (3–3.5φ or 91–125 μm; [49]) analysed for EY2010 and G2011 approach and overlap the distribution of vesicle sizes. Importantly, this observation highlights the need to consider the interplay between grain size and bubbles size in controlling SP measurements of volcanic ash, particularly when selecting grain size class(es) for analysis (Section 5.3).

5.2. The influence of bubbles on shape parameter measurements

Bubbles are an important control on ash particle morphology, particularly in determining their surface characteristics [49,51,56,57,68,75]. In 2-D, the intersection of vesicles with the exterior surfaces of ash particles produces concavities in the particle outline. For particles of a given size, the fraction of the total surface area composed of vesicle concavities will be controlled by the size and spatial distribution of bubbles in the melt prior to fragmentation (e.g. [49,56,68]). To examine further the relation between bubble size, abundance, particle size and particle shape parameters, we have created a series of synthetic ash particles comprising either squares or circles (of equal bubble-free area). We then systematically vary the size and abundance of perimeter-intersecting vesicles, and plot these synthetic ash particles on a SLD–CVX diagram (Fig. 10) for direct comparison with Fig. 8.

(a) *Changing the number of concavities of constant size:* For particles of constant size (where size is defined as either the circular diameter or the edge length of a square), the convexity decreases as the number of vesicle indentations increases (green symbols; Fig. 10a); this reflects the additional perimeter added to the particle by the vesicle indentations compared to the perimeter of the fully convex form. Note that the trend defined by the green symbols is not aligned parallel to the figure axes because of an intrinsic relationship between solidity and convexity, whereby perimeter cannot be increased entirely independently of the particle area, and vice versa.

(b) *Single concavities of changing size:* Increasing the size of a single vesicle indentation (again, for particles of constant size) produces a much greater change in solidity than convexity (blue

Fig. 10. Interpreting convexity and solidity using simplified geometries. (a) Synthetic ash shapes of equivalent area varying the number (green symbols), size (blue symbols), size and number (red symbols) or shape (orange symbols) of perimeter concavities. Note that digitisation of a curved outline results in values slightly <1 for a fully compact circle; this effect is minimised by a high pixel density (square = 57,600 pxls/p; circle = 45425 pxls/p). (b) As (a), but with the fields of different ash samples from Fig. 8a (dashed lines) and Fig. 8b (shaded) superimposed for comparison. The shaded regions correspond to shards (red), vesicular particles (green), dense fragments (blue), and microcrystalline vesicular particles (orange). (For interpretation of the references to colour in this figure legend, the reader is referred to the web version of this article.)

symbols; Fig. 10a). Importantly, the blue particles document a progressive increase in the size of the indentation *relative to the particle size,* and are therefore also equivalent to increasing the particle size for a constant size of perimeter concavity (see Section 5.3). Here, the reduction in solidity records area removed from the particle compared to the fully convex form. When compared to the effect of indentation number (green particles), increasing the size of a single concavity reduces the particle area by a much greater amount for comparable increases in perimeter.

(c) *Changing the shape of concavities:* Irregularly-shaped indentations comprising chains of small overlapping circles (representative of coalesced or deformed vesicles) increase the particle perimeter considerably for very little reduction in area (orange symbols; Fig. 10a).

(d) *Changing the size and number of concavities:* Increasing both the number of vesicle indentations and their size relative to that of the particle results in the lowest values of solidity (red symbols; Fig. 10a) where the area lost to concave indentations represents >>50% of the total convex hull area (i.e., particle size approaches the bubble size). Including multiple vesicle sizes further reduces both solidity and convexity. In contrast, increasing the number of indentations but decreasing their size relative to that of the particle results in some of the highest values of solidity (purple symbols; Fig. 10a), with a difference in area of <20% between the particle and its convex hull (i.e., particle size much greater than the bubble size).

The synthetic ash shapes encompass the range of ash morphologies observed in eruption deposits, albeit with simplified geometries. By overlaying the shape data for each ash component from Fig. 8b (shaded regions), we observe a good correlation between natural ash particles and the synthetic shapes to which they are morphologically most similar (Fig. 10b):

(a) *Glassy bubble shards* (red shading) represent the melt interstices between closely-spaced bubbles and therefore have most affinity to the red synthetic particles (from Fig. 10a), sharing similar low solidity values.

(b) *Glassy vesicular grains* (green shading), which by definition comprise numerous vesicles much smaller than the particle size, resemble more closely the green synthetic particles, and again plot in a similar region of the diagram.

(c) *Microcrystalline vesicular particles* (orange shading) are most similar to the orange synthetic ash shapes, which have narrow, convoluted indentations. This polylobate, interconnected vesicle texture is commonly observed in microlite-rich ash particles (or tachylite; e.g. [46,84]), where vesicles are deformed around crystal boundaries.

(d) *Dense fragments* (blue shading) derive from brittle fragmentation of poorly-vesicular melt and therefore lack perimeter concavities; these particles are close approximations of the fully convex shape and are characterised by high values of both solidity and convexity.
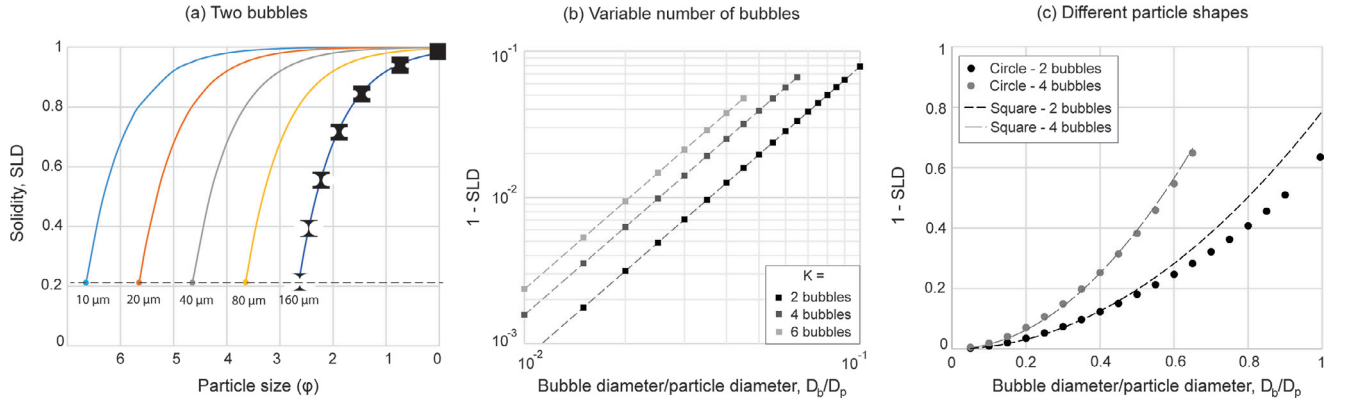
To summarise, the spatial distribution of particles on a SLD–CVX diagram is determined by the size, shape and abundance of perimeter-concavities. Morphological trends observed in natural ash samples can be reproduced using simplified synthetic ash shapes, whereby different ash 'components' can be described quantitatively in terms of their perimeter concavities. With some knowledge of what is controlling particle shape (e.g., vesicles), shape parameters can therefore be linked directly to specific morphologies.

5.3. Particle size considerations

The synthetic ash shapes shown in Fig. 10 highlight the effect of concavity size on solidity; as the sizes of intersecting bubbles increase relative to the particle size, the difference in area between the particle and its convex hull increases accordingly. Physically, a solidity value of 0.5 corresponds to 50% of the convex hull area occupied by perimeter concavities.

To place quantitative constraints on the relationship between ash particle shape and size, we consider the simplified geometry of circular bubbles intersecting square/circular particles (where the particle represents the interstice between two or more bubbles). We derive dimensionless formulae for solidity as a function of particle size, particle shape (squares and circles), bubble size and the number of bubbles (Fig. 11). We assume that the intersecting bubbles are (1) perfectly circular, (2) cut at their maximum 2-D cross-section, and (3) centred on the particle perimeter. When bubbles intersect square particles, solidity varies as

$$SLD = 1 - \frac{B_n \pi \left(\frac{D_b}{D_p}\right)^2}{8} \tag{2}$$

Fig. 11. Particle size considerations; (a) Solidity (SLD) as a function of particle size (*x*-axis) and bubble size (lines) for the simplified case of circles (bubbles) intersecting square particles (Eq. (2)). (b) Dimensionless relationship between SLD (shown as 1 − SLD to isolate D_b/D_p in Eq. (2) and the ratio of bubble size to particle size, for different numbers of intersecting bubbles; (c) Variation in SLD for bubbles intersecting different particle shapes – squares (dashed lines), and circles (symbols; Eqs. (3.1)–(3.3)).

where B_n refers to the number of intersecting bubbles and D_p and D_b refer to the particle length and bubble diameter, respectively. SLD values are non-unique, and can result from various permutations of bubbles and particle sizes (Fig. 11a). As particle size decreases, the same value of solidity can be maintained by decreasing the bubble size proportionally. Restricting bubbles to be centred on the particle perimeter imposes a minimum SLD (of 0.215 for 2 bubbles intersecting a square). The theoretical relationship between SLD and the ratio of the bubble diameter to the particle diameter (D_b/D_p) follows a power law distribution, with an exponent of 2 (Fig. 11b). Increasing the number of intersecting vesicles does not affect the exponent, but reduces SLD for a given D_b/D_p ratio.

Similarly, when the particle is circular solidity also varies systematically with D_b/D_p as

$$\text{SLD} = \frac{\left(\pi R^2 - B_n\left[R^2\cos^{-1}\left(\frac{d_1}{R}\right) - d_1\sqrt{R^2 - d_1^2}\right]\right) - \left(B_n\left(\left[r^2\cos^{-1}\left(\frac{d_2}{r}\right) - d_2\sqrt{r^2 - d_2^2}\right]\right)\right)}{\pi R^2 - B_n\left(R^2\cos^{-1}\left(\frac{d_1}{R}\right) - d_1\sqrt{R^2 - d_1^2}\right)} \tag{3.1}$$

$$d_1 = \frac{2R^2 - r^2}{2R} \tag{3.2}$$

$$d_2 = \frac{r^2}{2R} \tag{3.3}$$

where B_n refers to the number of intersecting bubbles, and R and r refer to the particle and bubble diameters, respectively. To avoid overestimating particle roughness, it is important in the case of circular particles to correct for the reduction in the convex hull area (A_{ch}) with increasing D_b/D_p. Geometrical constraints on intersecting circles again impose a minimum SLD, which becomes greater as the number of intersecting bubbles increases. When intersecting bubbles are small relative to the particle, circular particles follow the same power law relationship as squares. With increasing bubble size, SLD values for circles deviate from the power law relationship, such that for a particular D_b/D_p ratio the SLD of a circle will be higher (more regular) than for the equivalent square particle (Fig. 11c). This discrepancy between circles and squares becomes negligible as the number of intersecting bubbles increases. The divergence between different particle shapes is caused by the change in A_{ch} with increasing D_b/D_p for circles, which is most prominent for the case of two intersecting bubbles. As the number of intersecting bubbles increases, however, the convex hull of a circle approaches that of a square.

These observations using simple geometric shapes have important implications for the interpretation of morphological data. Firstly, it is clear that SP values cannot be ascribed uniquely to specific particle geometries; it is necessary to consider the dimensions of both

the particle and its constituent vesicles. A decrease in solidity, for example, could result from either reducing the particle size for a constant vesicle size, or increasing the vesicle size for a constant particle size. This non-uniqueness must be taken into account when applying genetic SP thresholds that have been calibrated using a particular dataset (e.g., magmatic vs. hydromagmatic; [10,58]) to other ash samples that may differ in their underlying bubble size distribution (BSD).

Secondly, solidity varies systematically as a function of the D_b/D_p ratio and, to a lesser degree, the number of bubbles. From Eqs. (2) and (3.1)–(3.3), quantitative constraints on the BSD can be obtained directly from shape measurements of known particle sizes. BSDs in volcanic systems are typically limited in their size range, and yet the grain size of volcanic pyroclasts can vary over many orders of magnitude [15]. For the simple case of two bubbles intersecting a square particle, changes in SLD are not significant until $D_b/D_p > {\sim}0.2$. Therefore, whilst the SLD of a 500 μm particle will be significantly reduced only for intersecting bubbles >100 μm, the SLD of a 100 μm particle will be influenced by any bubbles >20 μm. As the control of the BSD on ash shape will vary depending on the size fraction analysed, it may be possible to infer the modal bubble size directly from measurements of particle shape as a function of size [49].

To illustrate more clearly the relationships between particle size, bubble size, and particle shape, we overlay onto our diagram of synthetic ash shapes the fields of the different ash samples shown in Fig. 8a (dotted outlines; Fig. 10b). Bubble sizes in selected pumices from the 1980 eruption of Mt St Helens (MSH) range from 10 μm to 1 mm, with the modal bubble size between 10 and 90 μm [70] or between 10 and 22 μm (from bubble volumes; [30]). The shapes of the MSH ash particles (orange dashed line, Fig. 10b) are from the 250–500 μm sieve size (particle size ≫ bubble size), and therefore bubbles have only a minor effect on solidity. As convexity, however, is far more sensitive to irregularity at this scale, these samples plot in the high SLD, mid/low CVX region of the SLD–CVX diagram. In contrast, MSH ash particles <100 μm are dominated by highly concave bubble shards (not shown; [13]), which would exhibit much lower SLD values. Similarly, comparing the shapes of Surtsey ash particles within the 250–500 μm size fraction (blue dashed line, Fig. 10b) to those 90–125 μm in size (unpublished data of the authors; blue dotted line, Fig. 10b), we observe that the range of SLD expands to encompass

much lower values as particle size decreases. These two examples are consistent with an increase in the proportion of bubble shards relative to vesicular grains as particle size approaches the size of constituent bubbles. A similar relationship between grain size, bubble size and particle shape was documented in detail for the G2011 ash deposits [49]. Notably, dense fragments plot in a similar region of the SLD–CVX diagram regardless of the grain size analysed (Fig. 10b). In the absence of vesicles, ash particle shape therefore appears independent of size, consistent with fractal fragmentation theory (e.g., [40,43]).

6. Conclusions

Shape parameters provide quantitative, meaningful and reproducible measurements of particle morphology, if chosen carefully. By highlighting the shape properties that dominate the variance within a particle population, cluster analysis allows an objective selection of optimal shape parameters. Volcanic ash morphology is controlled primarily by the intersection of bubbles with the particle surface; differences in the shape, number density, and size of bubbles can account for much of the morphological diversity seen both within and between ash samples. The bubble textures observed in ash grains are determined by both the magma composition and the conditions of magma ascent (e.g., decompression rate, crystallisation, shearing), and in this way ash morphology can be related to the pre-fragmentation conditions. Shape parameters referenced to the convex hull are effective discriminators as they quantify surface roughness independently of particle form. Co-variation in convexity and solidity can distinguish between different ash components – dense fragments, bubble shards, vesicular particles, and microcrystalline grains – based on characteristic bubble properties. The overall shape distribution for a bulk sample will reflect the relative proportions of different juvenile components (plus non-juvenile material). The ability to identify components based on shape parameter measurements and determine their relative proportions offers a rapid, reproducible, and objective approach to sample componentry.

Importantly, however, the interaction between particle and bubble size distributions in volcanic systems means that shape measurements are inherently non-unique. For example, decreasing the particle size for a constant bubble size or increasing the bubble size for particles of a constant size can both result in the same reduction in solidity. Dimensionless relationships between particle size, bubble size, and particle shape can be determined theoretically for simplified, but realistic, ash geometries. These relationships have important implications for the interpretation of shape data, and, more fundamentally, for the selection of grain size(s) for analysis. When shape measurements are compared between different particle size fractions, differences may not be used uniquely to identify the underlying fragmentation mechanism. For this reason, the use of a single grain size fraction has been advocated by several authors: 0φ (<1 mm; [18]), 1φ (500 μm–1 mm; [17]), 1.5φ (350–500 μm; [57]), 2φ (250–500 μm; [47,51,56]), or 4φ (63–125 μm; [21,22,58]). However, the lack of consensus regarding the optimal grain size to analyse currently prevents direct comparison between the results of different studies. We emphasise that, wherever possible, analysing a range of grain size fractions (e.g. [19,49]) to determine variation in shape as a function of size not only ensures data intercomparability, but also provides valuable information regarding the controls on fragmentation, particularly when these data are compared to other measured ash properties such as bubble or crystal size distributions. Although the intrinsic relationship between particle size, bubble size and particle shape introduces challenges to inferring fragmentation style directly from shape measurements, this relationship can be used constructively to derive important information on the bubble size distribution (e.g., approximate modal and

maximum bubble sizes) based on variation in particle shape as a function of size.

The relationship between particle shape and bubble texture also has important implications for aerodynamic behaviour, particularly when the bubble size is large relative to the particle (e.g., bubble shards). The settling velocity of a flat bubble-shard will be significantly slower than a dense sphere of equivalent volume; irregular particles may therefore be more likely to travel further [1,4,7,19,52,69,82,92]. Theoretical settling velocities calculated using the spherical assumption differ by up to 50% when compared to those incorporating a shape correction [1,52], with the true ash particle diameters 10–120% larger than those of ideal spheres for a given terminal velocity [69]. Componentry of G2011 fall deposits show empirically that the proportion of irregular bubble shards and vesicular particles increased relative to dense blocky fragments with increasing dispersal distance from 50–115 km [49]. Morphological irregularity may account for the greater dispersal distances of fine ash than predicted by classical settling laws [7,21,82]. Importantly, the shape distribution of a particular grain size fraction measured at a single locality will be subject to some degree of shape-dependent sorting, and this will vary depending on the initial shape distribution of erupted pyroclasts. This potential morphological bias must be taken into account when using ash morphology to inform interpretations of eruptive processes, and offers another reason to characterise multiple grain size fractions.

Acknowledgements

Supplementary Materials

Supplementary material associated with this article can be found, in the online version, at doi:10.1016/j.grj.2015.09.001. The shape analysis macro for ImageJ, used for all shape measurements in this study, has been made available in the online supplementary materials.

References

[1] Alfano F, Bonadonna C, Delmelle P, Costantini L. Insights on tephra settling velocity from morphological observations. J Volcanol Geotherm Res 2011;208(3–4):86–98. doi:10.1016/j.jvolgeores.2011.09.013.

[2] Andronico D, Scollo S, Lo Castro MD, Cristaldi A, Lodato L, Taddeucci J. Eruption dynamics and tephra dispersal from the 24 November 2006 paroxysm at South-East Crater, Mt Etna, Italy. J Volcanol Geotherm Res 2014;274:78–91. doi:10.1016/j.jvolgeores.2014.01.009.

[3] Aschenbrenner BC. A new method of expressing particle sphericity. J Sediment Petrol 1956;26:15–31.

[4] Bagheri GH, Bonadonna C, Manzella I, Vonlanthen P. On the characterization of size and shape of irregular particles. Powder Technol 2015;270:141–53. doi:10.1016/j.powtec.2014.10.015.

[5] Barrett PJ. The shape of rock particles, a critical review. Sedimentology 1980;27(3):291–303. doi:10.1111/j.1365-3091.1980.tb01179.x.

[6] Bayhurst GK, Wohletz KH, Mason AS. A method for characterizing volcanic ash from the December 15, 1989, eruption of Redoubt Volcano, Alaska. Volcanic Ash and Aviation Safety: US Geological Survey Bulletin 1994;2047:13–18.

[7] Beckett FM, Witham CS, Hort MC, Stevenson JA, Bonadonna C, Millington SC. The sensitivity of NAME forecasts of the transport of volcanic ash clouds to the physical characteristics assigned to the particles; 2014. Forecasting research technical report, no. 592.

[8] Blott SJ, Pye K. Particle shape: a review and new methods of characterization and classification. Sedimentology 2008;55(1):31–63. doi:10.1111/j.1365-3091.2007.00892.x.

[9] Bjørk TE, Mair K, Austrheim H. Quantifying granular material and deformation: Advantages of combining grain size, shape, and mineral phase recognition analysis. J Struct Geol 2009;31(7):637–53.

[10] Büttner R, Dellino P, Raue H, Sonder I, Zimanowski B. Stress-induced brittle fragmentation of magmatic melts: theory and experiments. J Geophys Res-Sol Ea 2006;111(B8). doi:10.1029/2005jb003958.

[11] Corey AT. Influence of Shape on Fall Velocity of Sand Grains. Unpublished MSc Thesis, Colorado A&M College; 1949. p. 102.

[12] Carey S, Maria A, Sigurdsson H. Use of fractal analysis for discrimination of particles from primary and reworked jökulhlaup deposits in SE Iceland. J Volcanol Geotherm Res 2000;104(1):65–80.

[13] Carey SN, Sigurdsson H. Influence of particle aggregation on deposition of tephra from the May 18, 1980, eruption of Mount St-Helens volcano. J Geophys Res 1982;87(NB8):7061–72. doi:10.1029/JB087iB08p07061.

[14] Cashman KV, Fiske RS. Fallout of pyroclastic debris from submarine volcanic eruptions. Science 1991;253(5017):275–80. doi:10.1126/science.253.5017.275.

[15] Cashman KV, Sparks RSJ. How volcanoes work: a 25 year perspective. Geol Soc Am Bull 2013;125(5-6):664–90. doi:10.1130/b30720.1.

[16] Chappill JA. Quantitative characters in phylogenetic analysis. Cladistics—Int J Willi Hennig Soc 1989;5(3):217–34. doi:10.1111/j.1096-0031.1989.tb00487.x.

[17] Cioni R, D'Oriano C, Bertagnini A. Fingerprinting ash deposits of small scale eruptions by their physical and textural features. J Volcanol Geotherm Res 2008;177(1):277–87.

[18] Cioni R, Pistolesi M, Bertagnini A, Bonadonna C, Hoskuldsson A, Scateni B. Insights into the dynamics and evolution of the 2010 Eyjafjallajökull summit eruption (Iceland) provided by volcanic ash textures. Earth Planet Sci Lett 2014;394:111–23. doi:10.1016/j.epsl.2014.02.051.

[19] Coltelli M, Miraglia L, Scollo S. Characterization of shape and terminal velocity of tephra particles erupted during the 2002 eruption of Etna volcano, Italy. Bull Volcanol 2008;70(9):1103–12. doi:10.1007/s00445-007-0192-8.

[20] Cox EP. A method of assigning numerical and percentage values to the degree of roundness of sand grains. J Paleontol 1927;1(3):179–83.

[21] Dellino P, Gudmundsson MT, Larsen G, Mele D, Stevenson JA, Thordarson T, et al. Ash from the Eyjafjallajökull eruption (Iceland): fragmentation processes and aerodynamic behavior. J Geophys Res-Sol Ea 2012;117. doi:10.1029/2011jb008726.

[22] Dellino P, LaVolpe L. Image processing analysis in reconstructing fragmentation and transportation mechanisms of pyroclastic deposits. The case of Monte Pilato-Rocche Rosse eruptions, Lipari (Aeolian Islands, Italy). J Volcanol Geotherm Res 1996;71(1):13–29. doi:10.1016/0377-0273(95)00062-3.

[23] Dellino P, Mele D, Bonasia R, Braia G, La Volpe L, Sulpizio R. The analysis of the influence of pumice shape on its terminal velocity. Geophys Res Lett 2005;32(21). doi:10.1029/2005gl023954.

[24] Dioguardi F, Mele D. A new shape dependent drag correlation formula for non-spherical rough particles. Experiments and results. Powder Technol 2015;277:222–30.

[25] Duerig T, Mele D, Dellino P, Zimanowski B. Comparative analyses of glass fragments from brittle fracture experiments and volcanic ash particles. Bull Volcanol 2012;74(3):691–704. doi:10.1007/s00445-011-0562-0.

[26] Dufek J, Manga M, Patel A. Granular disruption during explosive volcanic eruptions. Nat Geosci 2012;5(8):561–4.

[27] Durant AJ, Rose WI, Sarna-Wojcicki AM, Carey S, Volentik ACM. Hydrometeor-enhanced tephra sedimentation: constraints from the 18 May 1980 eruption of Mount St. Helens. J Geophys Res-Sol Ea 2009;114. doi:10.1029/2008jb005756.

[28] Ersoy O, Gourgaud A, Aydar E, Chinga G, Thouret J-C. Quantitative scanning-electron microscope analysis of volcanic ash surfaces: application to the 1982–1983 Galunggung eruption (Indonesia). Geol Soc Am Bull 2007;119(5–6):743–52. doi:10.1130/b26048.1.

[29] Ganser GH. A rational approach to drag prediction of spherical and nonspherical particles. Powder Technol 1993;77(2):143–52. doi:10.1016/0032-5910(93)80051-b.

[30] Genareau K, Proussevitch AA, Durant AJ, Mulukutla G, Sahagian DL. Sizing up the bubbles that produce very fine ash during explosive volcanic eruptions. Geophys Res Lett 2012;39(15).

[31] Gislason SR, Hassenkam T, Nedel S, Bovet N, Eiriksdottir ES, Alfredsson HA, et al. Characterization of Eyjafjallajökull volcanic ash particles and a protocol for rapid risk assessment. Proc Natl Acad Sci USA 2011;108(18):7307–12. doi:10.1073/pnas.1015053108.

[32] Hentschel ML, Page NW. Selection of descriptors for particle shape characterization. Part Part Syst Char 2003;20(1):25–38. doi:10.1002/ppsc.200390002.

[33] Heiken G. Morphology and petrography of volcanic ashes. Geol Soc Am Bull 1972;83(7):1961–88.

[34] Heiken G, Wohletz K. Volcanic ash. Chicago, Harvard & MIT: University Presses of California; 1985.

[35] Heilbronner R, Barrett S. Image analysis in earth sciences: microstructures and textures of earth materials. Berlin, Heidelberg: Springer; 2014. doi:10.1007/978-3-642-10343-8.

[36] Heilbronner R, Keulen N. Grain size and grain shape analysis of fault rocks. Tectonophysics 2006;427(1):199–216.

[37] Herwegh M, De Bresser JHP, Ter Heege JH. Combining natural microstructures with composite flow laws: an improved approach for the extrapolation of lab data to nature. J Struct Geol 2005;27(3):503–21.

[38] Hone DWE, Mahony SH, Sparks RSJ, Martin KT. Cladistic analysis applied to the classification of volcanoes. Bull Volcanol 2007;70(2):203–20. doi:10.1007/s00445-007-0132-7.

[39] Jordan SC, Duerig T, Cas RAF, Zimanowski B. Processes controlling the shape of ash particles: results of statistical IPA. J Volcanol Geotherm Res 2014;288:19–27. doi:10.1016/j.jvolgeores.2014.09.012.

[40] Kaminski E, Jaupart C. The size distribution of pyroclasts and the fragmentation sequence in explosive volcanic eruptions. J Geophys Res-Sol Ea (1978–2012) 1998;103(B12):29759–79.

[41] Komar PD, Reimers CE. Grain shape effects on settling rates. J Geol 1978:193–209.

[42] Krumbein WC. The effects of abrasion on the size, shape and roundness of rock fragments. J Geol 1941;49(5):482–520.

[43] Kueppers U, Perugini D, Dingwell DB. "Explosive energy" during volcanic eruptions from fractal analysis of pyroclasts. Earth Planet Sci Lett 2006;248(3):800–7.

[44] Kulu P, Tümanok A, Mikli V, Käerdi H, Kohutek I, Besterci M. Possibilities of evaluation of powder particle granulometry and morphology by image analysis. Proc Eston Acad Sci Eng 1998;4:3–17.

[45] Kylling A, Kahnert M, Lindqvist H, Nousiainen T. Volcanic ash infrared signature: porous non-spherical ash particle shapes compared to homogeneous spherical ash particles. Atmos Meas Tech 2014;7(4):919–29. doi:10.5194/amt-7-919-2014.

[46] Lautze NC, Houghton BF. Linking variable explosion style and magma textures during 2002 at Stromboli volcano, Italy. Bull Volcanol 2007;69(4):445–60. doi:10.1007/s00445-006-0086-1.

[47] Leibrandt S, Le Pennec JL. Towards fast and routine analyses of volcanic ash morphometry for eruption surveillance applications. J Volcanol Geotherm Res 2015;297:11–27.

[48] Liu EJ, Cashman KV, Beckett FM, Witham CS, Leadbetter SJ, Hort MC, et al. Ash mists and brown snow: remobilization of volcanic ash from recent Icelandic eruptions. J Geophys Res-Atmos 2014;119(15):9463–80. doi:10.1002/2014jd021598.

[49] Liu EJ, Cashman KV, Rust AC, Gislason SR. The role of bubbles in generating fine ash during hydromagmatic eruptions. Geology 2015;43(3):239–42. doi:10.1130/g36336.1.

[50] Manga M, Patel A, Dufek J. Rounding of pumice clasts during transport: field measurements and laboratory studies. Bull Volcanol 2011;73(3):321–33. doi:10.1007/s00445-010-0411-6.

[51] Maria A, Carey S. Quantitative discrimination of magma fragmentation and pyroclastic transport processes using the fractal spectrum technique. J Volcanol Geotherm Res 2007;161(3):234–46. doi:10.1016/j.jvolgeores.2006.12.006.

[52] Mele D, Dellino P, Sulpizio R, Braia G. A systematic investigation on the aerodynamics of ash particles. J Volcanol Geotherm Res 2011;203(1-2):1–11. doi:10.1016/j.jvolgeores.2011.04.004.

[53] Merikallio S, Muñoz O, Sundström AM, Virtanen TH, Horttanainen M, Leeuw GD, et al. Optical modeling of volcanic ash particles using Ellipsoids. J Geophys Res Atmos 2015;120. doi:10.1002/2014JD022792.

[54] Mikli V, Kaerdi H, Kulu P, Besterci M. Characterization of powder particle morphology. Proc Eston Acad Sci Eng 2001;7(1):22–34.

[55] Mishler BD. Cladistic analysis of molecular and morphological data. Am J Phys Anthropol 1994;94(1):143–56. doi:10.1002/ajpa.1330940111.

[56] Miwa T, Shimano T, Nishimura T. Characterization of the luminance and shape of ash particles at Sakurajima volcano, Japan, using CCD camera images. Bull Volcanol 2015;77(1). doi:10.1007/s00445-014-0886-7.

[57] Miwa T, Toramaru A. Conduit process in vulcanian eruptions at Sakurajima volcano, Japan: inference from comparison of volcanic ash with pressure wave and seismic data. Bull Volcanol 2013;75(1):1–13.

[58] Murtagh RM, White JDL. Pyroclast characteristics of a subaqueous to emergent Surtseyan eruption, Black Point volcano, California. J Volcanol Geotherm Res 2013;267:75–91. doi:10.1016/j.jvolgeores.2013.08.015.

[59] Nemeth K. Volcanic glass textures, shape characteristics and compositions of phreatomagmatic rock units from the Western Hungarian monogenetic volcanic fields and their implications for magma fragmentation. Cent Eur J Geosci 2010;2(3):399–419. doi:10.2478/v10085-010-0015-6.

[60] Nemeth K, Cronin SJ. Drivers of explosivity and elevated hazard in basaltic fissure eruptions: the 1913 eruption of Ambrym Volcano, Vanuatu (SW-Pacific). J Volcanol Geotherm Res 2011;201(1-4):194–209. doi:10.1016/j.jvolgeores.2010.12.007.

[61] Olsson J, Stipp SLS, Dalby KN, Gislason SR. Rapid release of metal salts and nutrients from the 2011 Grímsvötn, Iceland volcanic ash. Geochim Cosmochim Acta 2013;123:134–49. doi:10.1016/j.gca.2013.09.009.

[62] Pepe S, Solaro G, Ricciardi GP, Tizzani P. On the fractal dimension of the fallout deposits: a case study of the 79 AD Plinian eruption at Mt. Vesuvius. J Volcanol Geotherm Res 2008;177(1):288–99.

[63] Perugini D, Speziali A, Caricchi L, Kueppers U. Application of fractal fragmentation theory to natural pyroclastic deposits: insights into volcanic explosivity of the Valentano scoria cone (Italy). J Volcanol Geotherm Res 2011;202(3):200–10.

[64] Pimentel RA, Riggins R. The nature of cladistic data. Cladistics 1987;3(3):201–9.

[65] Pons MN, Vivier H, Belaroui K, Bernard-Michel B, Cordier F, Oulhana D, Dodds JA. Particle morphology: from visualisation to measurement. Powder Technol 1999;103(1):44–57.

[66] Polacci M, Papale P. The evolution of lava flows from ephemeral vents at Mount Etna: insights from vesicle distribution and morphological studies. J Volcanol Geotherm Res 1997;76(1):1–17.

[67] Raadnui S, Roylance BJ. The classification of wear particle shape. Lubr Eng 1995;51(5):432–7.

[68] Rausch J, Grobéty B, Vonlanthen P. Eifel maars: quantitative shape characterization of juvenile ash particles (Eifel Volcanic Field, Germany). J Volcanol Geotherm Res 2015;291:86–100.

[69] Riley CM, Rose WI, Bluth GJS. Quantitative shape measurements of distal volcanic ash. J Geophys Res-Sol Ea 2003;108(B10). doi:10.1029/2001jb000818.

[70] Rust AC, Cashman KV. Permeability controls on expansion and size distributions of pyroclasts. J Geophys Res-Solid Ea 2011;116. doi:10.1029/2011jb008494.

[71] Rust AC, Manga M, Cashman KV. Determining flow type, shear rate and shear stress in magmas from bubble shapes and orientations. J Volcanol Geotherm Res 2003;122(1-2):111–32. doi:10.1016/s0377-0273(02)00487-0.

[72] Russ JC. Computer-assisted microscopy. US A: Springer; 1990. doi:10.1007/978-1-4613-0563-7.

[73] Russ JC, Woods RP. The image processing handbook. J Comput Assist Tomogr 1995;19(6):979–81.

[74] Sarocchi D, Sulpizio R, Macías JL, Saucedo R. The 17 July 1999 block-and-ash flow (BAF) at Colima Volcano: new insights on volcanic granular flows from textural analysis. J Volcanol Geotherm Res 2011;204(1):40–56.

[75] Schipper CI. Submarine explosive volcanism at Lo'ihi Seamount, Hawai'i; 2010. Unpublished thesis.

[76] Shea T, Houghton BF, Gurioli L, Cashman KV, Hammer JE, Hobden BJ. Textural studies of vesicles in volcanic rocks: an integrated methodology. J Volcanol Geotherm Res 2010;190(3-4):271–89. doi:10.1016/j.jvolgeores.2009.12.003.

[77] Shimano T, Nishimura T, Chiga N, Shibasaki Y, Iguchi M, Miki D, et al. Development of an automatic volcanic ash sampling apparatus for active volcanoes. Bull Volcanol 2013;75(12):1–7.

[78] Sneed ED, Folk RL. Pebbles in the Lower Colorado River, Texas, a study in particle morphogenesis. J Geol 1958;66(2):114–50.

[79] Sparks RSJ. The dynamics of bubble formation and growth in magmas: a review and analysis. J Volcanol Geotherm Res 1978;3(1):1–37.

[80] Stachowiak GW. Numerical characterization of wear particles morphology and angularity of particles and surfaces. Tribol Int 1998;31(1):139–57.

[81] Stachowiak GP, Stachowiak GW, Podsiadlo P. Automated classification of wear particles based on their surface texture and shape features. Tribol Int 2008;41(1):34–43. doi:10.1016/j.triboint.2007.04.004.

[82] Stevenson JA, Millington SC, Beckett FM, Swindles GT, Thordarson T. Big grains go far: reconciling tephrochronology with atmospheric measurements of volcanic ash. Atmos Measur Tech Dis 2015;8(1):65–120. doi:10.5194/amtd-8-65-2015.

[83] Storti F, Balsamo F, Salvini F. Particle shape evolution in natural carbonate granular wear material. Terra Nova 2007;19(5):344–52.

[84] Taddeucci J, Pompilio M, Scarlato P. Monitoring the explosive activity of the July–August 2001 eruption of Mt. Etna (Italy) by ash characterization. Geophys Res Lett 2002;29(8):71.

[85] Vonlanthen P, Rausch J, Ketcham RA, Putlitz B, Baumgartner LP, Grobéty B. High-resolution 3D analyses of the shape and internal constituents of small volcanic ash particles: the contribution of SEM micro-computed tomography (SEM micro-CT). J Volcanol Geotherm Res 2015;293:1–12. doi:10.1016/j.jvolgeores.2014.11.016.

[86] Vossepoel AM, Smeulders AWM. Vector code probability and metrication error in the representation of straight lines of finite length. Comput Graph Image Proc 1982;20(4):347–64. doi:10.1016/0146-664x(82)90057-0.

[87] Wadell H. Volume, shape, and roundness of rock particles. J Geol 1932;40(5):443–51.

[88] Walker GPL, Croasdale R. Characteristics of some basaltic pyroclastics. Bull Volcanol 1971;35(2):303–17.

[89] Ward JHJR. Hierachical groupings to optimize an objective function. J Am Stat Assoc 1963;58:234–44.

[90] Wentworth CK. A scale of grade and class terms for clastic sediments. J Geol 1922;30(5):377–92.

[91] Williams EM. A method of indicating particle shape with one parameter. J Sediment Petrol 1965;35:993–6.

[92] Wilson L, Huang TC. Influence of shape on the atmospheric settling velocity of volcanic ash particles. Earth Planet Sci Lett 1979;44(2):311–24. doi:10.1016/0012-821x(79)90179-1.

[93] Wohletz KH. Mechanisms of hydrovolcanic pyroclast formation: grain-size, scanning electron microscopy, and experimental studies. J Volcanol Geotherm Res 1983;17(1):31–63.

[94] Zingg T. Beitrage zur Schotteranalyse. Schweiz Miner Pefrog Mitt 1935;15:38–140.